# A node-based uniform strain virtual element method for compressible and nearly incompressible elasticity

A. Ortiz-Bernardin[a,*], R. Silva-Valenzuela[a], S. Salinas-Fernández[b], N. Hitschfeld-Kahler[b], S. Luza[a], B. Rebolledo[a]

[a]*Computational and Applied Mechanics Laboratory, Department of Mechanical Engineering, Universidad de Chile, Av. Beauchef 851, Santiago 8370456, Chile.*
[b]*Department of Computer Science, Universidad de Chile, Av. Beauchef 851, Santiago 8370456, Chile.*

## Abstract

We propose a combined nodal integration and virtual element method for compressible and nearly incompressible elasticity, wherein the strain is averaged at the nodes from the strain of surrounding virtual elements. For the strain averaging procedure, a nodal averaging operator is constructed using a generalization to virtual elements of the node-based uniform strain approach for finite elements. We refer to the proposed technique as the node-based uniform strain virtual element method (NVEM). No additional degrees of freedom are introduced in this approach, thus resulting in a displacement-based formulation. A salient feature of the NVEM is that the stresses and strains become nodal variables just like displacements, which can be exploited in nonlinear simulations. Through several benchmark problems in compressible and nearly incompressible elasticity as well as in elastodynamics, we demonstrate that the NVEM is accurate, optimally convergent and devoid of volumetric locking.

*Keywords:* Virtual element method, Nodal integration, Strain averaging, Uniform strain, Linear elasticity, Volumetric locking

## 1. Introduction

The virtual element method [1] (VEM) is a generalization of the finite element method (FEM) for approximation of field variables on very general meshes formed by elements with arbitrary

---

*Corresponding author. Tel: +56 2 2978 4664, Fax: +56 2 2689 6057,
*Email address:* aortizb@uchile.cl (A. Ortiz-Bernardin)

number of edges/faces (convex or nonconvex polytopes) known as virtual elements. In brief, the method consists in the construction of an algebraic (exact) representation of the stiffness matrix without computation of basis functions (basis functions are *virtual*). In this process, a decomposition of the stiffness matrix into a consistency part and a stability part that ensures convergence of the method [2] is realized. Although the VEM is relatively modern technology, nowadays its development includes applications such as elastic and inelastic solids [3–11], elastodynamics [12, 13], finite deformations [14–22], contact mechanics [14, 23, 24], fracture mechanics [25–29], fluid mechanics [30–34], geomechanics [35, 36] and topology optimization [20, 37, 38].

For linear elasticity, which is the focus in this paper, with the displacement field as the only variable (displacement-based approach), the simplest virtual element provides a linear approximation of the displacement field. As it occurs in traditional linear displacement-based finite elements (for instance, three-node triangles and four-node quadrilaterals), severe stiffening is exhibited by these virtual elements when the material is close to being incompressible, which occurs when the Poisson's ratio approaches 1/2. This is a numerical artifact known as volumetric locking. Currently, there are various approaches to deal with this issue in the VEM literature (details are provided below). Most of them are generalizations of well-established FEM approaches to VEM. In this paper, we propose an approach for linear displacement-based virtual elements that is usable for compressible and nearly incompressible elasticity. In the proposed approach, the strain is averaged at the nodes from the strain of surrounding virtual elements, a technique that is very popular in meshfree and finite element nodal integration (nodal integration is discussed below) and results in locking-free formulations. The proposed method differs from existing virtual element methods for compressible and nearly incompressible elasticity in the following aspects:

- In the proposed approach, the volumetric locking is alleviated by the strain averaging at the nodes and the stabilization matrix chosen. No additional degrees of freedom are introduced in this approach, thus resulting in a displacement-based formulation. In the existing VEM approaches, the volumetric locking is alleviated by the B-bar formulation [7, 12], mixed formulation [39], enhanced strain formulation [9], hybrid formulation [40], nonconforming formulations [41–43], or addition of degrees of freedom related to the normal components of

the displacement field on the element's edges to satisfy the inf-sup condition [10].

- The strains and stresses in the proposed approach are projected to the nodes, thus becoming nodal quantities just like displacements, whereas in the existing approaches these are projected inside the elements, thus becoming element quantities.

Nodal integration can be traced back to the work of Beissel and Belytschko [44] for meshfree Galerkin methods, where nodal integration emerged as an alternative to Gauss integration to accelerate the numerical integration of the weak form integrals. The main difference between these two types of numerical integration is that in nodal integration the weak form integrals are sampled at the nodes, whereas in Gauss integration the integrals are numerically integrated in the interior of the elements using cubature. Thus, in nodal integration, the state and history-dependent variables in the weak form integrals naturally become nodal quantities, whereas in Gauss integration these variables become element quantities. The obvious advantages of nodal integration over Gauss integration can be summarized as follows. There are much less nodes than Gauss points in the mesh, which results in huge computational savings when nodal integration is employed. In nonlinear computations with nodally integrated weak form integrals, the state and history-dependent variables are tracked only at the nodes. This feature can be exploited to avoid mesh remapping of these variables in Lagrangian large deformation simulations with remeshing (see, for instance, [45]), which is not possible when Gauss integration is used.

After the work of Beissel and Belytschko [44] nodal integration attracted great interest from the meshfree community (e.g., see Refs. [46–56]) due to the improved robustness of this type of integration over cell-based Gauss integration. Even though nodal integration greatly improves the computational cost of meshfree Galerkin simulations, still there exists the computational burden of meshfree basis functions (e. g., moving least-squares [57, 58], reproducing kernel [59] and maximum-entropy [60–62] approximants), which includes the solution of an optimization problem and a neighbor search at every integration node. Besides, meshfree basis functions generally do not vanish on the boundary, which requires additional procedures to impose Dirichlet boundary conditions. Regarding finite elements, there are various nodal integration approaches that use some form of pressure or strain averaging at the nodes; for instance, the average nodal pressure tetrahedral

3

element [63], node-based uniform strain triangular and tetrahedral elements [64], the averaged nodal deformation gradient linear tetrahedral element [65], and the family of nodally integrated continuum elements (NICE) and its derivative approaches [66–69, 69–72]. Recently, the node-based uniform strain approach [64] was adopted in the nodal particle finite element method (N-PFEM) [73, 74].

Nodal integration is prone to instabilities, and thus it requires stabilization. Stabilization is also an important aspect within the theoretical framework of the VEM [1], and thus this represents the main connection between nodal integration and the virtual element method. A summary of the stability issue in nodal integration is provided in Ref. [45], where also a gradient-based stabilization is proposed for small and Lagrangian large deformation simulations.

The VEM allows direct imposition of Dirichlet boundary conditions and its computational cost is comparable to that of the finite element method [77]. In addition, it is equipped with a stabilization procedure like in nodal integration. Regarding its sensitivity to mesh distortions, several authors have reported very robust solutions under mesh distortions [5, 6, 12, 18, 78, 79] and highly nonconvex elements [7, 13, 21, 37]. Since the VEM provides approximations that are interpolatory, stiffness matrix stabilization, and robustness under mesh distortion without the computational burden of meshfree methods, it is our opinion that the VEM will play a key role in the development of robust nodal integration techniques, especially in extreme large deformations.

In Ref. [55], where a nodal integration for meshfree Galerkin methods is proposed, the meshfree stiffness matrix was nodally integrated at the Voronoi sites of a background Voronoi tessellation. To render the nodal integration consistent and stable, the nodally integrated meshfree stiffness matrix was constructed using a meshfree version of the consistency and stability virtual element stiffness matrix decomposition. The nodal integration at Voronoi sites, however, is not possible in the standard VEM because of the following two issues: (a) it requires the evaluation of basis functions from surrounding Voronoi sites at the edges of the Voronoi cell, which cannot be performed in the VEM, and (b) the Voronoi sites contain the degrees of freedom while the VEM requires the degrees of freedom at the vertices of the Voronoi cell. Therefore, to enable nodal integration in the

---

[1]Although stabilization-free virtual elements were recently proposed [75, 76].

standard VEM a different approach must be devised.

In this exploratory paper, a combined nodal integration and virtual element method is proposed using ideas taken from the node-based uniform strain approach of Dohrmann et al. [64] for finite elements, wherein the strain is averaged at the nodes from the strain of surrounding elements. We refer to the proposed approach as the node-based uniform strain virtual element method (NVEM). The governing equations for linear elastostatics are provided in Section 2. Section 3 summarizes the theoretical framework of the VEM for linear elasticity. The NVEM is developed in Section 4. Stabilizations for the NVEM are discussed in Section 5. In Section 6, the numerical behavior of the NVEM is examined through several benchmark problems in compressible and nearly incompressible elasticity, and is also assessed in linear elastodynamics. Some concluding remarks along with ongoing and future research directions are discussed in Section 7. To ease the reading of the equations, a list of main symbols used throughout the paper is provided in Appendix A.

## 2. Governing equations

Consider an elastic body that occupies the open domain $\Omega \subset \mathbb{R}^2$ and is bounded by the one-dimensional surface $\Gamma$ whose unit outward normal is $\mathbf{n}_\Gamma$. The boundary is assumed to admit decompositions $\Gamma = \Gamma_D \cup \Gamma_N$ and $\emptyset = \Gamma_D \cap \Gamma_N$, where $\Gamma_D$ is the Dirichlet boundary and $\Gamma_N$ is the Neumann boundary. The closure of the domain is $\overline{\Omega} = \Omega \cup \Gamma$. Let $\mathbf{u}(\mathbf{x}) : \overline{\Omega} \to \mathbb{R}^2$ be the displacement field at a point of the elastic body with position vector $\mathbf{x}$ when the body is subjected to external tractions $\mathbf{t}_N(\mathbf{x}) : \Gamma_N \to \mathbb{R}^2$ and body forces $\mathbf{b}(\mathbf{x}) : \Omega \to \mathbb{R}^2$. The imposed Dirichlet (essential) boundary conditions are $\mathbf{u}_D(\mathbf{x}) : \Gamma_D \to \mathbb{R}^2$. The boundary-value problem for linear elastostatics reads: find $\mathbf{u}(\mathbf{x}) : \overline{\Omega} \to \mathbb{R}^2$ such that

$$\boldsymbol{\nabla} \cdot \boldsymbol{\sigma} + \mathbf{b} = 0 \quad \text{in } \Omega, \tag{1a}$$

$$\mathbf{u} = \mathbf{u}_D \quad \text{on } \Gamma_D, \tag{1b}$$

$$\boldsymbol{\sigma} \cdot \mathbf{n}_\Gamma = \mathbf{t}_N \quad \text{on } \Gamma_N, \tag{1c}$$

where $\boldsymbol{\sigma}$ is the Cauchy stress tensor.

The Galerkin weak formulation of the above problem is: find $\mathbf{u}(\mathbf{x}) \in \mathcal{V}$ such that

$$a(\mathbf{u}, \mathbf{v}) = \ell(\mathbf{v}) \quad \forall \mathbf{v}(\mathbf{x}) \in \mathcal{W},$$

$$a(\mathbf{u}, \mathbf{v}) = \int_{\Omega} \boldsymbol{\sigma}(\mathbf{u}) : \boldsymbol{\varepsilon}(\mathbf{v}) \, d\mathbf{x}, \quad \ell(\mathbf{v}) = \int_{\Omega} \mathbf{b} \cdot \mathbf{v} \, d\mathbf{x} + \int_{\Gamma_N} \mathbf{t}_N \cdot \mathbf{v} \, ds, \tag{2}$$

where $\mathcal{V}$ denotes the space of admissible displacements and $\mathcal{W}$ the space of its variations, and $\boldsymbol{\varepsilon}$ is the small strain tensor that is given by

$$\boldsymbol{\varepsilon}(\mathbf{u}) = \frac{1}{2} \left( \mathbf{u} \otimes \boldsymbol{\nabla} + \boldsymbol{\nabla} \otimes \mathbf{u} \right). \tag{3}$$

## 3. Virtual element method for linear elasticity

The virtual element method (VEM) [1] is a generalization of the finite element method (FEM) that can deal with very general meshes formed by elements with arbitrary number of edges (convex or non-convex polygons); the mesh can even include elements with coplanar edges and collapsing nodes, and non-matching elements. In the VEM, the displacement field is decomposed into a polynomial part and other terms using a projection operator. Altogether, this procedure results in an algebraic construction of the element stiffness matrix without the explicit construction of basis functions (basis functions are *virtual*). The decomposition of the displacement field leads to the following decomposition of the virtual element stiffness matrix:

$$\mathbf{K}_E = \mathbf{K}_E^{\mathrm{c}} + \mathbf{K}_E^{\mathrm{s}}, \tag{4}$$

where $\mathbf{K}_E^{\mathrm{c}}$ is the consistency part of the element stiffness matrix, which provides consistency to the method (i.e., ensures patch test satisfaction), and $\mathbf{K}_E^{\mathrm{s}}$ is the stability part of the element stiffness matrix, which provides stability.

A brief summary of the VEM for linear elasticity is given next. All the derivations are presented at the element level. Concerning the element, the following notation is used: the element is denoted by $E$ and its boundary by $\partial E$. The area of the element is denoted by $|E|$. The number of edges/nodes of an element are denoted by $N_E^V$. The unit outward normal to the element boundary

6

in the Cartesian coordinate system is denoted by $\mathbf{n} = [n_1 \quad n_2]^\mathsf{T}$. Fig. 1 depicts an element with five edges ($N_E^V = 5$), where the edge $e_a$ of length $|e_a|$ and the edge $e_{a-1}$ of length $|e_{a-1}|$ are the element edges incident to node $a$, and $\mathbf{n}_a$ and $\mathbf{n}_{a-1}$ are the unit outward normals to these edges, respectively.
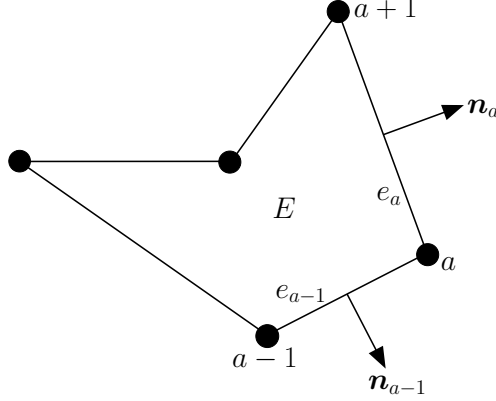


Fig. 1: Schematic representation of a polygonal element of $N_E^V = 5$ edges.

### 3.1. Projection operator

The fundamental procedure in the VEM is the decomposition of the displacement field into its polynomial part and some additional terms that are generally nonpolynomials. To this end, a projection operator $\Pi$ is defined such that

$$\mathbf{u}_h = \Pi\mathbf{u}_h + (\mathbf{u}_h - \Pi\mathbf{u}_h), \tag{5}$$

where $\mathbf{u}_h$ is the displacement approximation on the element (trial function), $\Pi\mathbf{u}_h$ is the polynomial part of $\mathbf{u}_h$ and $\mathbf{u}_h - \Pi\mathbf{u}_h$ contains the nonpolynomial terms of $\mathbf{u}_h$.

In this paper, we restrict ourselves to low-order approximations; that is, $\Pi$ is meant to project onto the space of linear polynomials. Let $\mathbf{x}_a = [x_{1a} \quad x_{2a}]^\mathsf{T}$ and $\mathbf{u}_a = [u_{1a} \quad u_{2a}]^\mathsf{T}$ be the coordinates and displacements of node $a$, respectively. At the element level, the projection operator onto the

linear displacements can be defined as [8, 55, 77, 80]

$$
\Pi\mathbf{u}_h = \begin{bmatrix} (x_1 - \bar{x}_1) & 0 & \frac{1}{2}(x_2 - \bar{x}_2) & 1 & 0 & \frac{1}{2}(x_2 - \bar{x}_2) \\ 0 & (x_2 - \bar{x}_2) & \frac{1}{2}(x_1 - \bar{x}_1) & 0 & 1 & -\frac{1}{2}(x_1 - \bar{x}_1) \end{bmatrix} \begin{bmatrix} \widehat{\varepsilon}_{11} \\ \widehat{\varepsilon}_{22} \\ 2\,\widehat{\varepsilon}_{12} \\ \bar{u}_1 \\ \bar{u}_2 \\ 2\,\widehat{\omega}_{12} \end{bmatrix}, \tag{6}
$$

where $\bar{x}_1$ and $\bar{x}_2$ are the components of the mean of the values that the position vector $\mathbf{x}$ takes over the vertices of the element; i.e.,

$$
\bar{\mathbf{x}} = \begin{bmatrix} \bar{x}_1 \\ \bar{x}_2 \end{bmatrix} = \frac{1}{N_E^V} \sum_{a=1}^{N_E^V} \mathbf{x}(\mathbf{x_a}), \tag{7}
$$

and $\bar{u}_1$ and $\bar{u}_2$ are the components of the mean of the values that the displacement $\mathbf{u}$ takes over the vertices of the element; i.e.,

$$
\bar{\mathbf{u}} = \begin{bmatrix} \bar{u}_1 \\ \bar{u}_2 \end{bmatrix} = \frac{1}{N_E^V} \sum_{a=1}^{N_E^V} \mathbf{u}(\mathbf{x}_a). \tag{8}
$$

In other words, $\bar{\mathbf{x}}$ and $\bar{\mathbf{u}}$ represents the geometric center of the element and its associated displacement vector, respectively; the terms $\widehat{\varepsilon}_{ij}$ are components of the element average $\widehat{\boldsymbol{\varepsilon}} = \frac{1}{|E|} \int_E \boldsymbol{\varepsilon} \, d\mathbf{x}$, and $\widehat{\omega}_{12}$ is the component of the element average $\widehat{\boldsymbol{\omega}} = \frac{1}{|E|} \int_E \boldsymbol{\omega} \, d\mathbf{x}$, where $\boldsymbol{\omega}$ is the skew-symmetric tensor that represents rotations. These element averages are evaluated on the boundary of $E$ by invoking the divergence theorem, which gives the following identities:

$$
\widehat{\boldsymbol{\varepsilon}}(\mathbf{u}_h) = \frac{1}{|E|} \int_E \boldsymbol{\varepsilon}(\mathbf{u}_h) \, d\mathbf{x} = \frac{1}{2|E|} \int_{\partial E} (\mathbf{u}_h \otimes \mathbf{n} + \mathbf{n} \otimes \mathbf{u}_h) \, ds, \tag{9}
$$

$$
\widehat{\boldsymbol{\omega}}(\mathbf{u}_h) = \frac{1}{|E|} \int_E \boldsymbol{\omega}(\mathbf{u}_h) \, d\mathbf{x} = \frac{1}{2|E|} \int_{\partial E} (\mathbf{u}_h \otimes \mathbf{n} - \mathbf{n} \otimes \mathbf{u}_h) \, ds. \tag{10}
$$

8

### 3.2. Discretization of field variables

Following a Galerkin approach, the element trial and test functions, $\mathbf{u}_h$ and $\mathbf{v}_h$, respectively, are assumed to be discretized as

$$\mathbf{u}_h = \begin{bmatrix} u_{1h} \\ u_{2h} \end{bmatrix} = \sum_{a=1}^{N_E^V} \phi_a(\mathbf{x})\mathbf{u}_a, \quad \mathbf{v}_h = \begin{bmatrix} v_{1h} \\ v_{2h} \end{bmatrix} = \sum_{a=1}^{N_E^V} \phi_a(\mathbf{x})\mathbf{v}_a, \tag{11}$$

where $\{\phi_a(\mathbf{x})\}_{a=1}^{N_E^V}$ are basis functions that form a partition of unity. Eqns. (8)–(10) reveal that all what is needed regarding the basis functions is the knowledge of their behavior on the element boundary. Thus, in the linear VEM the following behavior for the basis functions is assumed on the element boundary:

- basis functions are piecewise linear (edge by edge);

- basis functions are continuous on the element edges.

This means that the basis functions possess the Kronecker-delta property on the element edges, and hence they behave like the one-dimensional hat function.

When establishing the element matrices, we will see that these matrices are written in terms of the basis functions on the element boundary through (9) and the discretization of the displacements using (11). The element matrices will be then computed algebraically using the above assumptions in such a way that the basis functions are never computed. Thus, it is stressed that in the VEM the basis functions are not (and do not need to be) known explicitly.

### 3.3. VEM bilinear form

The projection operator (6) is derived[2] from the following orthogonality condition at the element level:

$$a_E(\mathbf{u}_h - \Pi\mathbf{u}_h, \mathbf{p}) = a_E(\mathbf{p}, \mathbf{v}_h - \Pi\mathbf{v}_h) = 0 \quad \forall \mathbf{p} \in [\mathcal{P}(E)]^2, \tag{12}$$

where $[\mathcal{P}(E)]^2$ is the space of linear displacements over the element. This orthogonality condition states that the nonpolynomial terms $\mathbf{u}_h - \Pi\mathbf{u}_h$ in $E$, measured in the energy norm, are orthogonal

---

[2]The derivation is given in Ref. [55]

to $[\mathcal{P}(E)]^2$. Using the decomposition (5) along with condition (12), and noting that $\Pi\mathbf{u}_h$ and $\Pi\mathbf{v}_h$ $\in [\mathcal{P}(E)]^2$, the following VEM representation of the bilinear form is obtained:

$$a_E(\mathbf{u}_h, \mathbf{v}_h) = a_E(\Pi\mathbf{u}_h, \Pi\mathbf{v}_h) + a_E(\mathbf{u}_h - \Pi\mathbf{u}_h, \mathbf{v}_h - \Pi\mathbf{v}_h). \tag{13}$$

The VEM bilinear form can be further elaborated. For convenience, the projection operator (6) is rewritten as

$$\Pi\mathbf{u}_h = \mathbf{h}(\mathbf{x})\widehat{\varepsilon}(\mathbf{u}_h) + \mathbf{g}(\mathbf{x})\mathbf{r}(\mathbf{u}_h), \tag{14}$$

where

$$\mathbf{h}(\mathbf{x}) = \begin{bmatrix} (x_1 - \bar{x}_1) & 0 & \frac{1}{2}(x_2 - \bar{x}_2) \\ 0 & (x_2 - \bar{x}_2) & \frac{1}{2}(x_1 - \bar{x}_1) \end{bmatrix}, \quad \mathbf{g}(\mathbf{x}) = \begin{bmatrix} 1 & 0 & \frac{1}{2}(x_2 - \bar{x}_2) \\ 0 & 1 & -\frac{1}{2}(x_1 - \bar{x}_1) \end{bmatrix}, \tag{15}$$

$$\mathbf{r}(\mathbf{u}_h) = \begin{bmatrix} \bar{u}_1 & \bar{u}_2 & 2\widehat{\omega}_{12} \end{bmatrix}^\mathsf{T}, \tag{16}$$

and

$$\widehat{\varepsilon}(\mathbf{u}_h) = \begin{bmatrix} \widehat{\varepsilon}_{11} & \widehat{\varepsilon}_{22} & 2\widehat{\varepsilon}_{12} \end{bmatrix}^\mathsf{T} \tag{17}$$

is the vector form of the element average strain. From now on, we always use this vector form when referring to the element average strain $\widehat{\varepsilon}$.

Using the bilinear form written in terms of the vector form of the strain — that is, $a(\mathbf{u}_h, \mathbf{v}_h) = \int_\Omega \varepsilon^\mathsf{T}(\mathbf{v}_h)\, \mathbf{D}\, \varepsilon(\mathbf{u}_h)\, d\mathbf{x}$, where $\mathbf{D}$ is the constitutive matrix — and noting that $\mathbf{r}(\mathbf{u}_h)$ represents rigid body translations and rotation, and that these do not produce strain energy, the first term on the right-hand side of (13) can be written, as follows:

$$\begin{aligned} a_E(\Pi\mathbf{u}_h, \Pi\mathbf{v}_h) &= \int_E \begin{bmatrix} \frac{\partial \Pi v_{1h}}{\partial x_1} & \frac{\partial \Pi v_{2h}}{\partial x_2} & \frac{\partial \Pi v_{1h}}{\partial x_2} + \frac{\partial \Pi v_{2h}}{\partial x_1} \end{bmatrix} \mathbf{D} \begin{bmatrix} \frac{\partial \Pi u_{1h}}{\partial x_1} \\ \frac{\partial \Pi u_{2h}}{\partial x_2} \\ \frac{\partial \Pi u_{1h}}{\partial x_2} + \frac{\partial \Pi u_{2h}}{\partial x_1} \end{bmatrix} d\mathbf{x} \\ &= \int_E \widehat{\varepsilon}^\mathsf{T}(\mathbf{v}_h)\, \mathbf{D}\, \widehat{\varepsilon}(\mathbf{u}_h)\, d\mathbf{x}. \end{aligned} \tag{18}$$

For an isotropic linear elastic material, the constitutive matrix is given by

$$\mathbf{D} = \frac{E_Y}{(1+\nu)(1-2\nu)} \begin{bmatrix} 1-\nu & \nu & 0 \\ \nu & 1-\nu & 0 \\ 0 & 0 & \frac{1-2\nu}{2} \end{bmatrix} \tag{19}$$

for plane strain condition, and

$$\mathbf{D} = \frac{E_Y}{1-\nu^2} \begin{bmatrix} 1 & \nu & 0 \\ \nu & 1 & 0 \\ 0 & 0 & \frac{1-\nu}{2} \end{bmatrix} \tag{20}$$

for plane stress condition, where $E_Y$ is the Young's modulus and $\nu$ is the Poisson's ratio.

The second term on the right-hand side of (13) can be written as

$$a_E(\mathbf{u}_h - \Pi\mathbf{u}_h, \mathbf{v}_h - \Pi\mathbf{v}_h) = (\mathbf{1} - \Pi)^{\mathsf{T}} a_E(\mathbf{v}_h, \mathbf{u}_h)(\mathbf{1} - \Pi), \tag{21}$$

which reveals that $a_E(\mathbf{u}_h - \Pi\mathbf{u}_h, \mathbf{v}_h - \Pi\mathbf{v}_h)$ is not computable since $a_E(\mathbf{v}_h, \mathbf{u}_h)$ would need to be evaluated inside the element using cubature, but the VEM basis functions are not known inside the element. However, since $a_E(\mathbf{u}_h - \Pi\mathbf{u}_h, \mathbf{v}_h - \Pi\mathbf{v}_h)$ is meant to only provide stability, $a_E(\mathbf{v}_h, \mathbf{u}_h)$ can be conveniently approximated by a bilinear form $s_E(\cdot, \cdot)$ that is computable while preserving the coercivity of the system. In other words, $s_E(\mathbf{v}_h, \mathbf{u}_h)$ must be positive definite and scale like $a_E(\cdot, \cdot)$ in the kernel of $\Pi$ [1, 8].

Using (18) and (21) with the approximation $a_E(\mathbf{v}_h, \mathbf{u}_h) = s_E(\mathbf{v}_h, \mathbf{u}_h)$, the VEM bilinear form for linear elasticity is written as

$$a_{h,E}(\mathbf{u}_h, \mathbf{v}_h) = \int_E \widehat{\boldsymbol{\varepsilon}}^{\mathsf{T}}(\mathbf{v}_h)\, \mathbf{D}\, \widehat{\boldsymbol{\varepsilon}}(\mathbf{u}_h)\, d\mathbf{x} + (\mathbf{1} - \Pi)^{\mathsf{T}} s_E(\mathbf{v}_h, \mathbf{u}_h)(\mathbf{1} - \Pi) \tag{22}$$

### 3.4. VEM element stiffness matrix

The discrete element average strain is computed using (11), as follows:

$$\widehat{\varepsilon}_h(\mathbf{u}_h) = \widehat{\varepsilon}\left(\sum_{a=1}^{N_E^V} \phi_a(\mathbf{x})\mathbf{u}_a\right) = \mathbf{B}\mathbf{d}, \tag{23}$$

where

$$\mathbf{d} = \begin{bmatrix} u_{11} & u_{21} & \cdots & u_{1a} & u_{2a} & \cdots & u_{1N_E^V} & u_{2N_E^V} \end{bmatrix}^{\mathsf{T}} \tag{24}$$

is the column vector of element nodal displacements and

$$\mathbf{B} = \begin{bmatrix} \mathbf{B}_1 & \cdots \mathbf{B}_a \cdots & \mathbf{B}_{N_E^V} \end{bmatrix}, \quad \mathbf{B}_a = \begin{bmatrix} q_{1a} & 0 \\ 0 & q_{2a} \\ q_{2a} & q_{1a} \end{bmatrix}, \tag{25}$$

where $q_{ia} = \frac{1}{|E|}\int_{\partial E} \phi_a(\mathbf{x})n_i\, ds$. Since the VEM basis functions are assumed to be piecewise linear (edge by edge) and continuous on the element boundary, $q_{ia}$ can be exactly computed using a trapezoidal rule, which gives the following algebraic expression:

$$q_{ia} = \frac{1}{2|E|}\left(|e_{a-1}|n_{i(a-1)} + |e_a|n_{ia}\right), \quad i = 1, 2, \tag{26}$$

where $n_{ia}$ is the $i$-th component of $\mathbf{n}_a$ and $|e_a|$ is the length of the edge incident to node $a$ as defined in Fig. 1. Using (23) and noting that $\widehat{\varepsilon}$ and $\mathbf{D}$ are constant over the element, the discrete version of the first term on the right-hand side of (22) is written as

$$\int_E \widehat{\varepsilon}_h^{\mathsf{T}}(\mathbf{v}_h)\, \mathbf{D}\, \widehat{\varepsilon}_h(\mathbf{u}_h)\, d\mathbf{x} = |E|\, \widehat{\varepsilon}_h^{\mathsf{T}}(\mathbf{v}_h)\, \mathbf{D}\, \widehat{\varepsilon}_h(\mathbf{u}_h) = \mathbf{q}^{\mathsf{T}}\left(|E|\mathbf{B}^{\mathsf{T}}\mathbf{D}\mathbf{B}\right)\mathbf{d}, \tag{27}$$

where $\mathbf{q}$ is a column vector similar to (24) that contains the element nodal values associated with $\mathbf{v}_h$.

To obtain the discrete version of the second term on the right-hand side of (22), the discretization of $\Pi$ is required. This demands the discretization of $h(\mathbf{x})$, $\widehat{\varepsilon}(\mathbf{u}_h)$, $g(\mathbf{x})$ and $r(\mathbf{u}_h)$. The

discretization of $\widehat{\varepsilon}(\mathbf{u}_h)$ is given in (23). The remainder terms are discretized, as follows:

$$\mathbf{h}_h(\mathbf{x}) = \sum_{a=1}^{N_E^V} \phi_a(\mathbf{x})\mathbf{h}(\mathbf{x}_a) = \mathbf{NH}, \tag{28}$$

$$\mathbf{g}_h(\mathbf{x}) = \sum_{a=1}^{N_E^V} \phi_a(\mathbf{x})\mathbf{g}(\mathbf{x}_a) = \mathbf{NG}, \tag{29}$$

$$\mathbf{r}_h = \mathbf{r}\left(\sum_{a=1}^{N_E^V} \phi_a(\mathbf{x})\mathbf{u}_a\right) = \mathbf{Rd}, \tag{30}$$

where

$$\mathbf{N} = \left[\begin{array}{ccccc} \mathbf{N}_1 & \cdots & \mathbf{N}_a & \cdots & \mathbf{N}_{N_E^V} \end{array}\right], \quad \mathbf{N}_a = \left[\begin{array}{cc} \phi_a(\mathbf{x}) & 0 \\ 0 & \phi_a(\mathbf{x}) \end{array}\right], \tag{31}$$

$$\mathbf{H} = \left[\begin{array}{c} \mathbf{H}_1 \\ \vdots \\ \mathbf{H}_a \\ \vdots \\ \mathbf{H}_{N_E^V} \end{array}\right], \quad \mathbf{H}_a = \left[\begin{array}{ccc} (x_{1a} - \bar{x}_1) & 0 & \frac{1}{2}(x_{2a} - \bar{x}_2) \\ 0 & (x_{2a} - \bar{x}_2) & \frac{1}{2}(x_{1a} - \bar{x}_1) \end{array}\right], \tag{32}$$

$$\mathbf{G} = \left[\begin{array}{c} \mathbf{G}_1 \\ \vdots \\ \mathbf{G}_a \\ \vdots \\ \mathbf{G}_{N_E^V} \end{array}\right], \quad \mathbf{G}_a = \left[\begin{array}{ccc} 1 & 0 & \frac{1}{2}(x_{2a} - \bar{x}_2) \\ 0 & 1 & -\frac{1}{2}(x_{1a} - \bar{x}_1) \end{array}\right], \tag{33}$$

and

$$\mathbf{R} = \left[\begin{array}{ccccc} \mathbf{R}_1 & \cdots & \mathbf{R}_a & \cdots & \mathbf{R}_{N_E^V} \end{array}\right], \quad \mathbf{R}_a = \left[\begin{array}{cc} \frac{1}{N_E^V} & 0 \\ 0 & \frac{1}{N_E^V} \\ q_{2a} & -q_{1a} \end{array}\right]. \tag{34}$$

Therefore, the discrete $\Pi$ can be written as

$$\Pi_h \mathbf{u}_h = \mathbf{N}\mathbf{H}\mathbf{B}\mathbf{d} + \mathbf{N}\mathbf{G}\mathbf{R}\mathbf{d} = \mathbf{N}(\mathbf{H}\mathbf{B} + \mathbf{G}\mathbf{R})\mathbf{d}, \tag{35}$$

which defines the projection matrix as

$$\mathbf{P} = \mathbf{H}\mathbf{B} + \mathbf{G}\mathbf{R}. \tag{36}$$

Using the projection matrix and the discrete field $\mathbf{u}_h = \sum_{a=1}^{N_E^V} \phi_a(\mathbf{x})\mathbf{u}_a = \mathbf{N}\mathbf{d}$, the discrete version of the second term on the right-hand side of (22) is

$$\mathbf{q}^\mathsf{T}(\mathbf{I} - \mathbf{P})^\mathsf{T} s_E(\mathbf{N}^\mathsf{T}, \mathbf{N})(\mathbf{I} - \mathbf{P})\mathbf{d} = \mathbf{q}^\mathsf{T}(\mathbf{I} - \mathbf{P})^\mathsf{T}\, \mathbf{S}\,(\mathbf{I} - \mathbf{P})\mathbf{d}. \tag{37}$$

Finally, using (27) and (37), the discrete VEM bilinear form is written as

$$a_{h,E}(\mathbf{u}_h, \mathbf{v}_h) = \mathbf{q}^\mathsf{T}\left\{ |E|\, \mathbf{B}^\mathsf{T}\, \mathbf{D}\, \mathbf{B} + (\mathbf{I} - \mathbf{P})^\mathsf{T}\, \mathbf{S}\,(\mathbf{I} - \mathbf{P}) \right\}\mathbf{d}, \tag{38}$$

which defines the element stiffness matrix as the sum of the element consistency stiffness matrix, $\mathbf{K}_E^\mathrm{c}$, and the element stability stiffness matrix, $\mathbf{K}_E^\mathrm{s}$, as follows:

$$\mathbf{K}_E = \mathbf{K}_E^\mathrm{c} + \mathbf{K}_E^\mathrm{s}, \quad \mathbf{K}_E^\mathrm{c} = |E|\, \mathbf{B}^\mathsf{T}\, \mathbf{D}\, \mathbf{B}, \quad \mathbf{K}_E^\mathrm{s} = (\mathbf{I} - \mathbf{P})^\mathsf{T}\, \mathbf{S}\,(\mathbf{I} - \mathbf{P}). \tag{39}$$

*3.5. VEM element force vector*

For linear fields, the VEM version of the loading term in the weak form (2) is computed at the element level, as follows [1, 3, 5]:

$$\ell_E^b(\mathbf{v}_h) = \int_E \widehat{\mathbf{b}} \cdot \bar{\mathbf{v}}_h\, d\mathbf{x} = |E|\, \widehat{\mathbf{b}} \cdot \bar{\mathbf{v}}_h, \quad \widehat{\mathbf{b}} = \frac{1}{|E|}\int_E \mathbf{b}\, d\mathbf{x}, \quad \bar{\mathbf{v}}_h = \frac{1}{N_E^V}\sum_{a=1}^{N_E^V} \mathbf{v}_h(\mathbf{x}_a) \tag{40}$$

14

for the loading term associated with the body forces, and similarly

$$\ell_e^t(\mathbf{v}_h) = |e|\,\widehat{\mathbf{t}}_N \cdot \bar{\mathbf{v}}_h, \quad \widehat{\mathbf{t}}_N = \frac{1}{|e|}\int_e \mathbf{t}_N\,ds, \quad \bar{\mathbf{v}}_h = \frac{1}{N_e^V}\sum_{a=1}^{N_e^V}\mathbf{v}_h(\mathbf{x}_a) \tag{41}$$

for the loading term associated with the tractions applied on an edge located on the Neumann boundary, where $e$ and $|e|$ are as defined in Fig. 1 and $N_e^V$ is the number of nodes of the edge. The discrete versions of these loading terms are $\ell_{h,E}^b(\mathbf{v}_h) = \mathbf{q}^\mathsf{T}\mathbf{f}_E^b$ and $\ell_{h,e}^t(\mathbf{v}_h) = \mathbf{q}^\mathsf{T}\mathbf{f}_e^t$, where $\mathbf{f}_E^b$ and $\mathbf{f}_e^t$ are the element force vectors given, respectively, by

$$\mathbf{f}_E^b = |E|\,\bar{\mathbf{N}}^\mathsf{T}\widehat{\mathbf{b}}, \tag{42}$$

where

$$\bar{\mathbf{N}} = \left[\begin{array}{ccccc} \bar{\mathbf{N}}_1 & \cdots & \bar{\mathbf{N}}_a & \cdots & \bar{\mathbf{N}}_{N_E^V} \end{array}\right], \quad \bar{\mathbf{N}}_a = \left[\begin{array}{cc} \frac{1}{N_E^V} & 0 \\ 0 & \frac{1}{N_E^V} \end{array}\right], \tag{43}$$

and

$$\mathbf{f}_e^t = |e|\,\bar{\mathbf{N}}_\Gamma^\mathsf{T}\widehat{\mathbf{t}}_N, \tag{44}$$

where

$$\bar{\mathbf{N}}_\Gamma = \left[\begin{array}{cccc} \frac{1}{N_e^V} & 0 & \frac{1}{N_e^V} & 0 \\ 0 & \frac{1}{N_e^V} & 0 & \frac{1}{N_e^V} \end{array}\right] = \left[\begin{array}{cccc} \frac{1}{2} & 0 & \frac{1}{2} & 0 \\ 0 & \frac{1}{2} & 0 & \frac{1}{2} \end{array}\right] \tag{45}$$

since the number of nodes of an edge is $N_e^V = 2$.

## 4. Node-based uniform strain virtual element method (NVEM)

The virtual element method for linear elasticity described in Section 3 is prone to volumetric locking in the limit $\nu \to 1/2$. Using the virtual element mesh and considering a typical nodal vertex $I$, we propose to use a nodal averaging operator $\pi_I$ in (13) that is designed to preclude volumetric locking without introducing additional degrees of freedom. This nodal averaging operator leads to a nodal version of the VEM bilinear form, as follows:

$$a_{h,I}(\mathbf{u}_h, \mathbf{v}_h) = a_I(\pi_I[\Pi\mathbf{u}_h], \pi_I[\Pi\mathbf{v}_h]) + s_I(\pi_I[\mathbf{u}_h - \Pi\mathbf{u}_h], \pi_I[\mathbf{v}_h - \Pi\mathbf{v}_h]), \tag{46}$$

15

where according to the VEM theory, $s_I(\pi_I[\mathbf{u}_h - \Pi\mathbf{u}_h], \pi_I[\mathbf{v}_h - \Pi\mathbf{v}_h])$ is a computable approximation to $a_I(\pi_I[\mathbf{u}_h - \Pi\mathbf{u}_h], \pi_I[\mathbf{v}_h - \Pi\mathbf{v}_h])$ and is meant to provide stability. The notations $a_I$ and $s_I$ are introduced as the nodal counterparts of the element bilinear form $a_E$ and its stabilization term $s_E$, respectively.

### 4.1. Construction of the nodal averaging operator

Each node of the mesh is associated with their own patch of virtual elements. The patch for node $I$ is denoted by $\mathcal{T}_I$ and is defined as the set of virtual elements connected to node $I$ (see Fig. 2). Each node of a virtual element $E$ in the patch is assigned the area $\frac{1}{N_E^V}|E|$; that is, the area of an element is uniformly distributed among its nodes. The representative area of node $I$ is denoted by $|I|$ and is computed by addition of all the areas that are assigned to node $I$ from the elements in $\mathcal{T}_I$; that is,

$$|I| = \sum_{E \in \mathcal{T}_I} \frac{1}{N_E^V}|E|. \tag{47}$$

Similarly, each node of a virtual element $E$ is uniformly assigned the strain $\frac{1}{N_E^V}\widehat{\boldsymbol{\varepsilon}}(\mathbf{u}_h)$. On considering each strain assigned to node $I$ from the elements in $\mathcal{T}_I$, we define the *node-based uniform strain*, as follows:

$$\widehat{\boldsymbol{\varepsilon}}_I(\mathbf{u}_h) = \frac{1}{|I|} \sum_{E \in \mathcal{T}_I} |E|\frac{1}{N_E^V}\widehat{\boldsymbol{\varepsilon}}(\mathbf{u}_h). \tag{48}$$

Since $\widehat{\boldsymbol{\varepsilon}}(\mathbf{u}_h)$ is by definition given at the element level, then from Eq. (48) the following nodal averaging operator is proposed:

$$\pi_I[\,\cdot\,] = \frac{1}{|I|} \sum_{E \in \mathcal{T}_I} |E|\frac{1}{N_E^V}[\,\cdot\,]_E, \tag{49}$$

where $[\,\cdot\,]_E$ denotes evaluation over the element $E$. Using this nodal averaging operator, the nodal representation of a function $F$ is obtained as

$$F_I = \pi_I[F] = \frac{1}{|I|} \sum_{E \in \mathcal{T}_I} |E|\frac{1}{N_E^V}[F]_E. \tag{50}$$

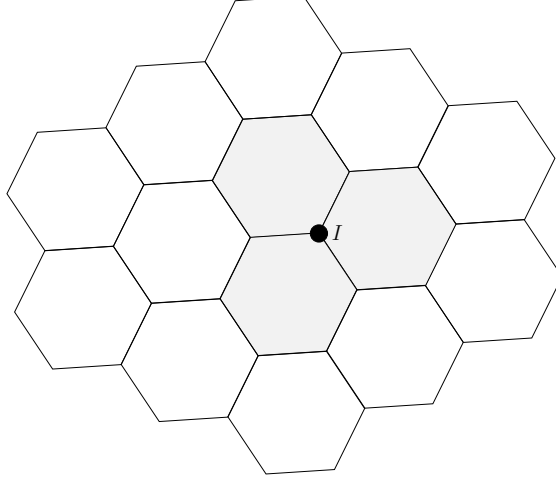The idea of having a nodal strain (like the one in (48)) that is representative of the nodal patch

16

Fig. 2: Nodal patch $\mathcal{T}_I$ (shaded elements) formed by the virtual elements that are connected to node $I$.

$\mathcal{T}_I$ has long been used in meshfree and finite element nodal integration techniques [45, 51, 63–67, 69, 70, 81]. In particular, the node-based uniform strain approach was developed for three-node triangular and four-node tetrahedral elements in Ref. [64], and proved to perform well for nearly incompressible solids. However, that approach presented stability issues in some particular instances and required stabilization [45]. Within the VEM framework, stabilization is obtained by construction of the method, and hence in combining the node-based uniform strain approach with the VEM no stability issues will arise (we demonstrate this through numerical experiments in Section 6).

### 4.2. NVEM bilinear form

Using the nodal averaging operator (49), the nodal representation of the VEM bilinear form for linear elasticity (Eq. (22)) is written as

$$a_{h,I}(\mathbf{u}_h, \mathbf{v}_h) = |I|\, \widehat{\boldsymbol{\varepsilon}}_I^{\mathsf{T}}(\mathbf{v}_h)\, \mathbf{D}\, \widehat{\boldsymbol{\varepsilon}}_I(\mathbf{u}_h) + (\mathbf{1} - \Pi)_I^{\mathsf{T}} s_I(\mathbf{v}_h, \mathbf{u}_h)(\mathbf{1} - \Pi)_I. \tag{51}$$

Let $N$ be the total number of nodes in the mesh. The global bilinear form is obtained by summing through the $N$ nodes, as follows:

$$a_h(\mathbf{u}_h, \mathbf{v}_h) = \sum_{I=1}^{N} \left[ |I|\, \widehat{\boldsymbol{\varepsilon}}_I^{\mathsf{T}}(\mathbf{v}_h)\, \mathbf{D}\, \widehat{\boldsymbol{\varepsilon}}_I(\mathbf{u}_h) + (\mathbf{1} - \Pi)_I^{\mathsf{T}} s_I(\mathbf{v}_h, \mathbf{u}_h)(\mathbf{1} - \Pi)_I \right]. \tag{52}$$

17

*4.3. NVEM nodal stiffness matrix*

The nodal stiffness matrix that arises from (51) is the nodal version of (39). This gives

$$\mathbf{K}_I = \mathbf{K}_I^{\mathrm{c}} + \mathbf{K}_I^{\mathrm{s}}, \quad \mathbf{K}_I^{\mathrm{c}} = |I| \, \mathbf{B}_I^{\mathsf{T}} \, \mathbf{D} \, \mathbf{B}_I, \quad \mathbf{K}_I^{\mathrm{s}} = (\mathbf{I} - \mathbf{P})_I^{\mathsf{T}} \, \mathbf{S}_I \, (\mathbf{I} - \mathbf{P})_I, \tag{53}$$

where $\mathbf{B}_I = \pi_I[\mathbf{B}]$, $(\mathbf{I} - \mathbf{P})_I = \pi_I[\mathbf{I} - \mathbf{P}]$, and the stability matrix $\mathbf{S}_I$ is defined in Section 5.

*4.4. NVEM nodal force vector*

The nodal force vector associated with the body forces is the nodal representation of (42) and is given by

$$\mathbf{f}_I^b = |I| \, \bar{\mathbf{N}}_I^{\mathsf{T}} \widehat{\mathbf{b}}_I, \tag{54}$$

where $\bar{\mathbf{N}}_I = \pi_I[\bar{\mathbf{N}}]$ and $\widehat{\mathbf{b}}_I = \pi_I[\widehat{\mathbf{b}}]$. Similarly, the nodal force vector associated with the tractions is given by the nodal representation of (44), as follows:

$$\mathbf{f}_I^t = |I| \, \bar{\mathbf{N}}_{\Gamma,I}^{\mathsf{T}} \widehat{\mathbf{t}}_{N,I}, \tag{55}$$

where the nodal components are now computed with respect to the one-dimensional domain on the Neumann boundary; that is, $|I| = \sum_{e \in \mathcal{T}_I} \frac{1}{2}|e|$, where $e$ is an element's edge located on the Neumann boundary and $|e|$ its length; $\mathcal{T}_I$ now represents the set of edges connected to node $I$ on the Neumann boundary. Proceeding as mentioned, the remainder nodal matrices are

$$\bar{\mathbf{N}}_{\Gamma,I} = \frac{1}{|I|} \sum_{e \in \mathcal{T}_I} |e| \frac{1}{2} [\bar{\mathbf{N}}_\Gamma]_e, \tag{56}$$

and

$$\widehat{\mathbf{t}}_{N,I} = \frac{1}{|I|} \sum_{e \in \mathcal{T}_I} |e| \frac{1}{2} [\widehat{\mathbf{t}}_N]_e. \tag{57}$$

## 5. Stabilization for the node-based uniform strain virtual element method

Within the VEM framework, stabilization is one of the key ingredients to guarantee convergence. However, in nodal integration, stabilization can make the formulation somewhat stiff in the nearly

incompressible limit [51]. To mitigate this, a modified constitutive matrix $\widetilde{\mathbf{D}}$ can be used in lieu of the standard $\mathbf{D}$ when computing the stability matrix. We opt for $\widetilde{\mathbf{D}}$ given as follows [45]:

$$\widetilde{\mathbf{D}} = \mathbf{D}\big(\widetilde{E}, \widetilde{\nu}\big), \tag{58}$$

where

$$\widetilde{E} = \frac{\widetilde{\nu}\left(3\widetilde{\lambda} + 2\widetilde{\mu}\right)}{\widetilde{\lambda} + \widetilde{\mu}}, \quad \widetilde{\nu} = \frac{\widetilde{\lambda}}{2\left(\widetilde{\lambda} + \widetilde{\mu}\right)}; \tag{59}$$

$\widetilde{\lambda}$ and $\widetilde{\mu}$ are, respectively, the modified Lamé's first and second parameters, which are calculated as follows:

$$\widetilde{\mu} := \mu, \quad \widetilde{\lambda} := \min\left(\lambda, 25\widetilde{\mu}\right), \tag{60}$$

where $\lambda$ and $\mu$ are the Lamé parameters of the problem to solve. Similarly, another possibility to mitigate the stiff response is offered by the use of a modified constitutive matrix $\mathbf{D}_\mu$ given by

$$\mathbf{D}_\mu = \begin{bmatrix} 2\mu & 0 & 0 \\ 0 & 2\mu & 0 \\ 0 & 0 & \mu \end{bmatrix}, \tag{61}$$

which omits the pressure parameter $\lambda(\varepsilon_{11} + \varepsilon_{22})$ that is responsible of the possible stiff behavior. Alternatively, a simpler definition of $\mathbf{D}_\mu$ that produces practically identical results is obtained using the constitutive matrix that is related to the shear deformations; i.e.,

$$\mathbf{D}_\mu = \begin{bmatrix} 0 & 0 & 0 \\ 0 & 0 & 0 \\ 0 & 0 & \mu \end{bmatrix}. \tag{62}$$

We point out that the foregoing stabilization procedure with $\mathbf{D}_\mu$ as given in (62) is similar to one of the stabilization approaches in the B-bar VEM [7] (see Appendix A therein).

Using the modified constitutive matrices, we define the stability matrix as the nodal version of the *D-recipe* stabilization technique [78, 82]. This gives two diagonal stability matrices whose

19

entries are given by

$$(\mathbf{S}_I)_{i,i} = \max\left(1, \left(|I|\,\mathbf{B}_I^\mathsf{T}\,\widetilde{\mathbf{D}}\,\mathbf{B}_I\right)_{i,i}\right) \tag{63}$$

and

$$(\mathbf{S}_I)_{i,i} = \max\left(1, \left(|I|\,\mathbf{B}_I^\mathsf{T}\,\mathbf{D}_\mu\,\mathbf{B}_I\right)_{i,i}\right). \tag{64}$$

We refer to (63) and (64), respectively, as $\widetilde{\mathbf{D}}$ and $\mathbf{D}_\mu$ stabilizations.

## 6. Numerical experiments

In this section, numerical experiments are conducted to demonstrate the accuracy, convergence and stability of the NVEM for compressible and nearly incompressible linear elastostatics. In addition, the performance of the NVEM in linear elastodynamics is also demonstrated. For the elastostatic numerical experiments, the numerical results are compared with the B-bar VEM [7] and the standard linear VEM. For the elastodynamic numerical experiments, the numerical results are compared with the finite element method (FEM) using eight-node quadrilateral elements (Q8).

To assess the convergence of the numerical solution of the NVEM approach, we use the nodal values of the exact displacement, strain and pressure fields, that is, $\mathbf{u}(\mathbf{x}_I)$, $\boldsymbol{\varepsilon}(\mathbf{x}_I)$ and $p(\mathbf{x}_I)$, respectively, and define the following nodal errors at node $I$:

$$\mathbf{e}_u = \mathbf{u}(\mathbf{x}_I) - \mathbf{u}_I, \quad \mathbf{e}_\varepsilon = \boldsymbol{\varepsilon}(\mathbf{x}_I) - \widehat{\boldsymbol{\varepsilon}}_I \quad e_p = p(\mathbf{x}_I) - p_I,$$

where $\mathbf{u}_I$, $\widehat{\boldsymbol{\varepsilon}}_I$ and $p_I = -\lambda\,\mathrm{trace}\,(\widehat{\boldsymbol{\varepsilon}}_I)$ are the nodal values of the displacement, strain and pressure fields approximations, respectively. Using the nodal errors, the following norms are evaluated through nodal integration in the NVEM approach:

$$\frac{\|\mathbf{u}(\mathbf{x}) - \mathbf{u}_h(\mathbf{x})\|_{L^2(\Omega)}}{\|\mathbf{u}(\mathbf{x})\|_{L^2(\Omega)}} = \sqrt{\frac{\sum_{I=1}^{N}\mathbf{e}_u^\mathsf{T}\mathbf{e}_u\,|I|}{\sum_{I=1}^{N}\mathbf{u}^\mathsf{T}(\mathbf{x}_I)\,\mathbf{u}(\mathbf{x}_I)\,|I|}},$$

$$\frac{\|\mathbf{u}(\mathbf{x}) - \mathbf{u}_h(\mathbf{x})\|_{H^1(\Omega)}}{\|\mathbf{u}(\mathbf{x})\|_{H^1(\Omega)}} = \sqrt{\frac{\sum_{I=1}^{N}\mathbf{e}_\varepsilon^\mathsf{T}\,\mathbf{D}\,\mathbf{e}_\varepsilon\,|I|}{\sum_{I=1}^{N}\boldsymbol{\varepsilon}^\mathsf{T}(\mathbf{x}_I)\,\mathbf{D}\,\boldsymbol{\varepsilon}(\mathbf{x}_I)\,|I|}},$$

$$\frac{\|p(\mathbf{x}) - p_h(\mathbf{x})\|_{L^2(\Omega)}}{\|p(\mathbf{x})\|_{L^2(\Omega)}} = \sqrt{\frac{\sum_{I=1}^{N} e_p^{\mathsf{T}} e_p |I|}{\sum_{I=1}^{N} p^{\mathsf{T}}(\mathbf{x}_I) p(\mathbf{x}_I) |I|}}.$$

For the standard VEM and the B-Bar VEM approaches, the above norms are evaluated using cubature inside the element through partition of the element into triangles and the errors defined at the element level as $\mathbf{e}_u = \mathbf{u}(\mathbf{x}) - \Pi \mathbf{u}_h(\mathbf{x})$, $\mathbf{e}_\varepsilon = \boldsymbol{\varepsilon}(\mathbf{x}) - \widehat{\boldsymbol{\varepsilon}}_h(\mathbf{u}_h)$ and $e_p = p(\mathbf{x}) - p_h(\mathbf{x})$, where $p_h(\mathbf{x}) = -\lambda \operatorname{trace}(\widehat{\boldsymbol{\varepsilon}}_h(\mathbf{u}_h))$.

### 6.1. Patch test and numerical stability

With dimensions in inches, we investigate the accuracy and numerical stability of the proposed NVEM approach by solving displacement patch tests and eigenvalue analyses on the meshes shown in Fig. 3 for the square domain $\Omega = (0,1)^2$. In both problems $\mathbf{b} = \mathbf{0}$ lbf/in$^3$ and plane strain condition is assumed with the following material parameters: $E = 1 \times 10^7$ psi and $\nu = 0.3$. For the displacement patch test, the Dirichlet boundary condition $\mathbf{u}_D = \{x_1 \quad x_1 + x_2\}^{\mathsf{T}}$ in inches is prescribed along the entire boundary of the domain. Numerical results for the relative error in the $L^2$ norm and the $H^1$ seminorm are presented in Tables 1 and 2, respectively, where it is confirmed that the patch test is met to machine precision.

The eigenvalue analyses delivers three zero eigenvalues, which corresponds to the three zero-energy rigid body modes. The three mode shapes that follow the three rigid body modes are depicted in Fig. 4 for the distorted mesh. These mode shapes are smooth, which is an indication of the numerical stability of the method.

Table 1: Relative error in the $L^2$ norm for the displacement patch tests.

| Method | Regular | Distorted |
|---|---|---|
| NVEM, $\widetilde{\mathbf{D}}$ | $7.8 \times 10^{-16}$ | $9.7 \times 10^{-16}$ |
| NVEM, $\mathbf{D}_\mu$ | $4.8 \times 10^{-16}$ | $3.9 \times 10^{-16}$ |

### 6.2. Colliding flow

We consider a simple model of colliding flow, which is a well-known standard benchmark problem (for example, see Refs. [83]) that is described by the Stokes equations. Since the Stokes flow
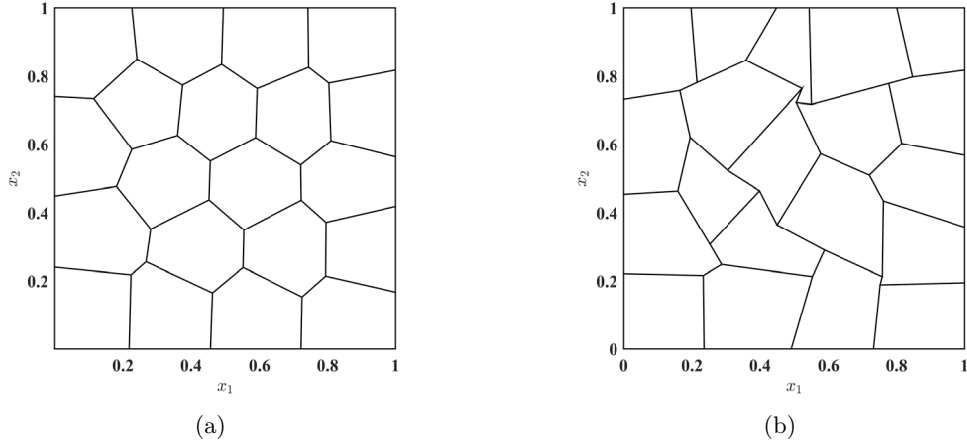
Fig. 3: Meshes used for the displacement patch tests and numerical stability. (a) Regular mesh and (b) distorted mesh.

Table 2: Relative error in the $H^1$ seminorm for the displacement patch tests.

| Method | Regular | Distorted |
|--------|---------|-----------|
| NVEM, $\widetilde{\mathbf{D}}$ | $5.9 \times 10^{-16}$ | $8.2 \times 10^{-16}$ |
| NVEM, $\mathbf{D}_\mu$ | $8.0 \times 10^{-16}$ | $6.6 \times 10^{-16}$ |

equations coincide with the equations that govern the static incompressible elasticity, the colliding flow can be solved using the linear elastostatic model with the following constitutive matrix:

$$\mathbf{D} = \begin{bmatrix} \lambda + 2\mu & \lambda & 0 \\ \lambda & \lambda + 2\mu & 0 \\ 0 & 0 & \mu \end{bmatrix},$$

where the Lamé parameters are set to $\lambda = 5 \times 10^7$ psi and $\mu = 1$ psi, which results in a Poisson's ratio $\nu = 0.49999999$. For dimensions in inches, the problem is defined on the square domain $\Omega = (0,2)^2$ and Dirichlet boundary conditions are imposed along the entire boundary of the domain using the
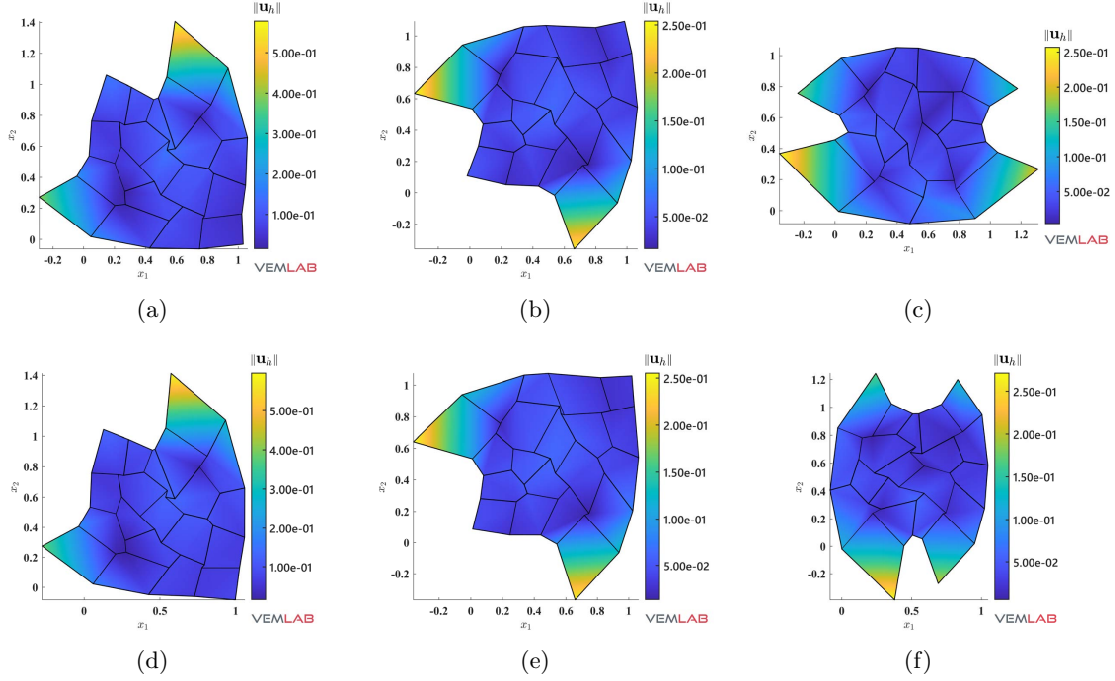
Fig. 4: Eigenvalue analyses on the distorted mesh. A pictorial of the three mode shapes that follow the three rigid body modes. (a)–(c) NVEM with $\widetilde{\mathbf{D}}$ stabilization and (d)–(f) NVEM with $\mathbf{D}_\mu$ stabilization.

following analytical solution [83]:

$$u_1 = 20(x_1 - 1)(x_2 - 1)^3 \tag{65a}$$

$$u_2 = 5(x_1 - 1)^4 - 5(x_2 - 1)^4 \tag{65b}$$

$$p = 60(x_1 - 1)^2(x_2 - 1) - 20(x_2 - 1)^3, \tag{65c}$$

where $u_1$ and $u_2$ are the components of the velocity field $\mathbf{u}$ in inches, and $p$ is the pressure field in psi. The stabilizations presented in Section 5 are considered to assess the convergence of the method upon mesh refinement. A sample polygonal mesh used in the convergence study is shown in Fig. 5.

We start by showing the need for stability in the NVEM approach. Fig. 6 presents a comparison between unstabilized and stabilized solutions for the nodal fields $\|\mathbf{u}_h\|$ and $p_h$ — scatter plots are used for the NVEM as in this approach the field variables are known at the nodes. The unstabilized solutions exhibit marked spurious oscillations at the corners $(0,0)$ and $(2,0)$ (Figs. 6(a) and 6(c)),

23
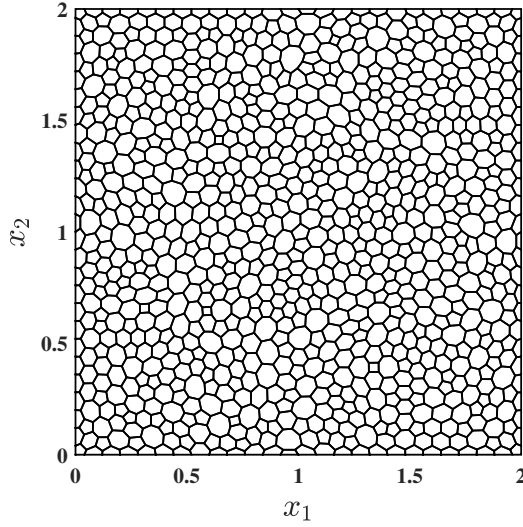
Fig. 5: Sample mesh for the colliding flow problem.

whereas the stabilized solutions become smooth on the whole domain (Figs. 6(b) and 6(d)).

The convergence and accuracy of the NVEM with $\widetilde{\mathbf{D}}$ and $\mathbf{D}_\mu$ stabilizations are demonstrated in Fig. 7, where the $L^2$ norm and the $H^1$ seminorm of the displacement error, and the $L^2$ norm of the pressure error indicate accurate solutions with optimal convergence rates of 2, 1 and 1, respectively. In comparison with the B-bar VEM approach, which is also accurate and optimally convergent, the NVEM approach is slightly more accurate in the $H^1$ seminorm of the displacement error and the $L^2$ norm of the pressure error. Finally, as expected, in these convergence plots the standard VEM solution behaves very inaccurate due to volumetric locking.

*6.3. Cantilever beam subjected to a parabolic end load*

With dimensions in inches, a cantilever beam of unit thickness whose domain of analysis is $\Omega = (0,8) \times (-2,2)$ is subjected to a parabolic end load $P$ that is applied on the edge $x = 8$. The Dirichlet boundary conditions are applied on the edge $x = 0$ according to the following exact solution given by Timoshenko and Goodier [84] for plane strain state:

$$u_1 = -\frac{Px_2}{6\overline{E}_Y I} \left( (6L - 3x_1)x_1 + (2 + \overline{\nu})x_2^2 - \frac{3D^2}{2}(1 + \overline{\nu}) \right),$$
$$u_2 = \frac{P}{6\overline{E}_Y I} \left( 3\overline{\nu}x_2^2(L - x_1) + (3L - x_1)x_1^2 \right)$$
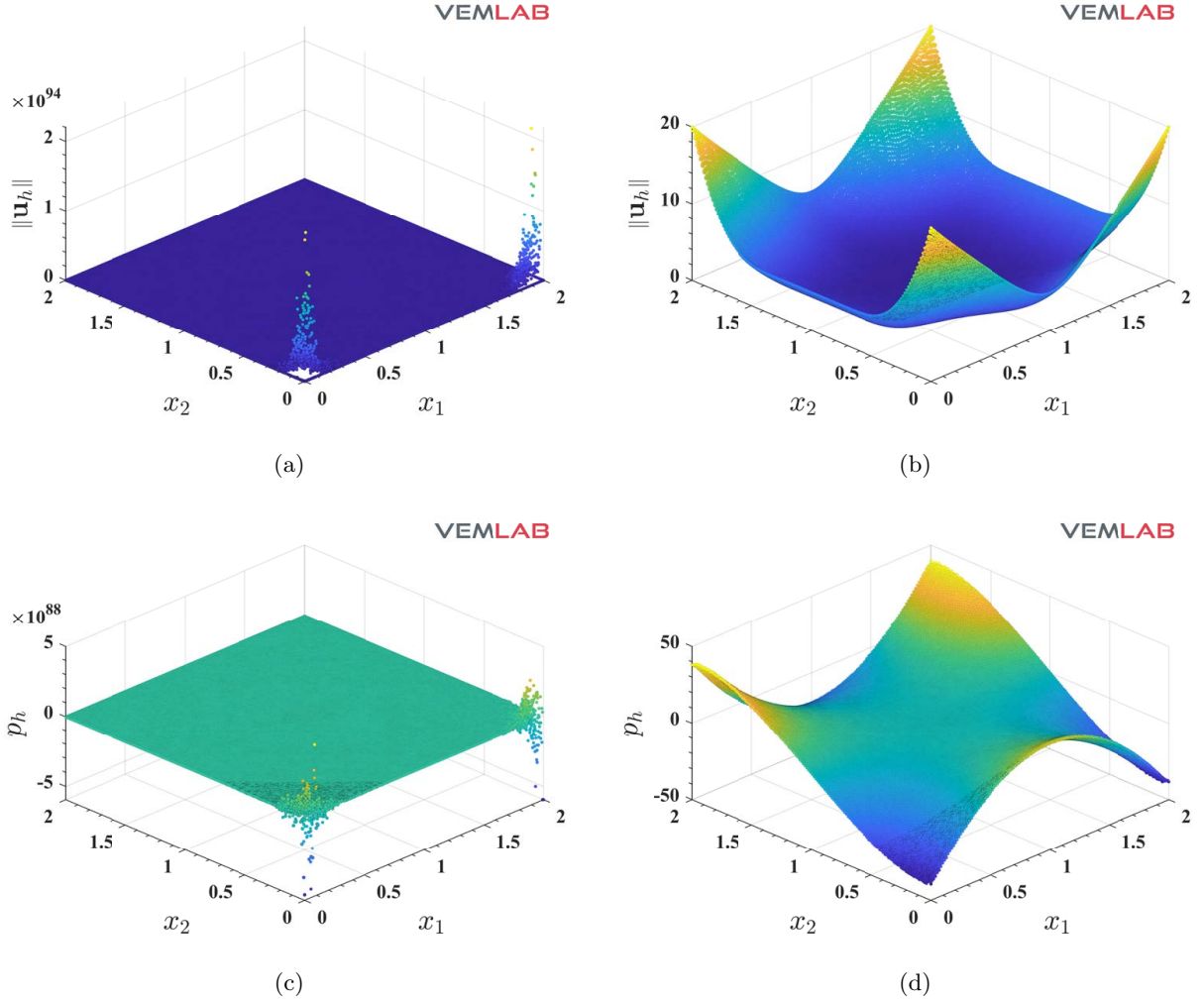
Fig. 6: Comparison between unstabilized and stabilized solutions in the NVEM for the colliding flow problem. (a) Unstabilized $\|\mathbf{u}_h\|$ (in), (b) stabilized $\|\mathbf{u}_h\|$ (in), (c) unstabilized $\|p_h\|$ (psi) and (d) stabilized $\|p_h\|$ (psi).

with $\overline{E}_Y = E_Y / \left(1 - \nu^2\right)$ and $\overline{\nu} = \nu / \left(1 - \nu\right)$, where $E_Y$ and $\nu$ are the Young's modulus and the Poisson's ratio of the linear elastic material, respectively; $L$ is the length of the beam, $D$ is the height of the beam, and $I$ is the second-area moment of the beam section. The total load on the Neumann boundary is $P = -1000$ lbf. The geometry and boundary conditions, and a sample polygonal mesh used in this study are shown in Fig. 8.

The convergence and accuracy of the NVEM is studied for two sets of material parameters. The first set is $E = 10^7$ psi and $\nu = 0.3$ (compressible elasticity), and the second set is $E = 10^7$ psi and $\nu = 0.499999$ (nearly incompressible elasticity).
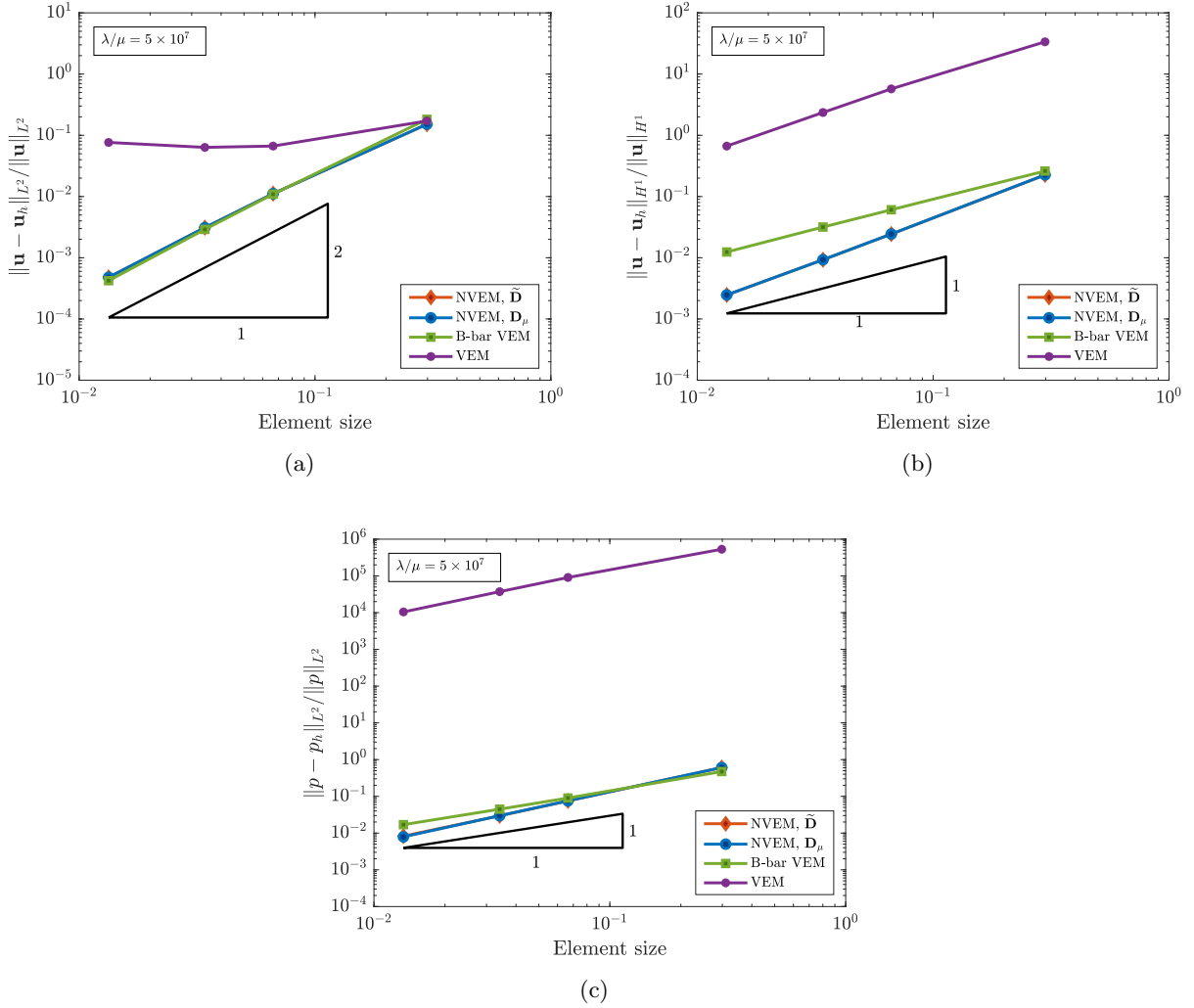
Fig. 7: Colliding flow problem. Convergence rates in the (a) $L^2$ norm of the displacement error, (b) $H^1$ seminorm of the displacement error and (c) $L^2$ norm of the pressure error for the VEM, B-bar VEM and NVEM.

### 6.3.1. Compressible elasticity

For compressible elasticity, Fig. 9 presents the $L^2$ norm and the $H^1$ seminorm of the displacement error, and the $L^2$ norm of the pressure error, where it is observed that accurate solutions with optimal convergence rates of 2, 1 and 1, respectively, are delivered by the NVEM with $\widetilde{\mathbf{D}}$ and $\mathbf{D}_\mu$ stabilizations. The VEM and the B-bar VEM also exhibit accurate solutions with optimal rates of convergence. In comparison with the VEM and the B-bar VEM, the NVEM is more accurate in the $H^1$ seminorm of the displacement error and the $L^2$ norm of the pressure error, whereas less accurate in the $L^2$ norm of the displacement error.
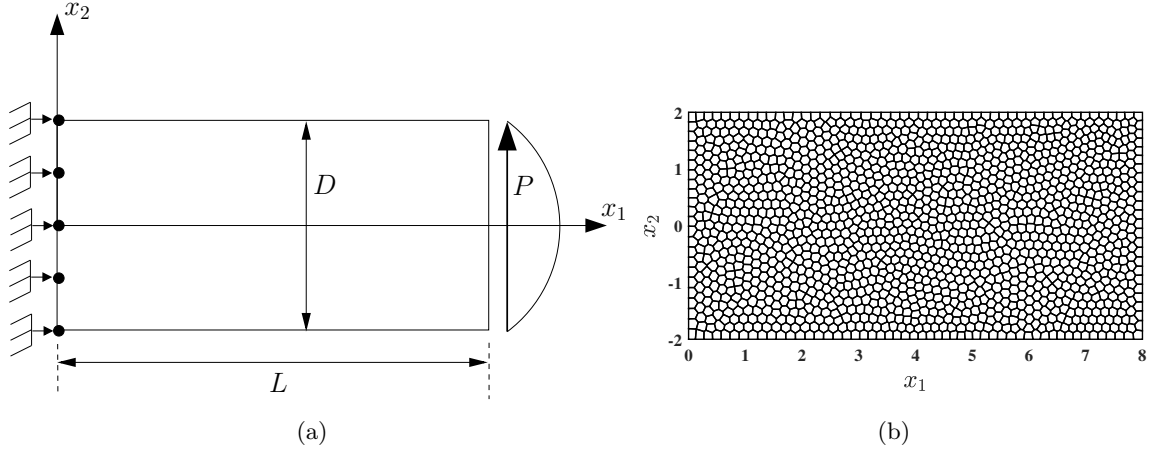
Fig. 8: Cantilever beam (a) geometry and boundary conditions, and (b) a sample mesh.

### 6.3.2. Nearly incompressible elasticity

For nearly incompressible elasticity, the NVEM and the B-bar VEM are accurate and optimally convergent, as shown in Fig. 10. Like in the compressible case, the NVEM is more accurate than the B-bar VEM in the $H^1$ seminorm of the displacement error and the $L^2$ norm of the pressure error, whereas less accurate in the $L^2$ norm of the displacement error. As expected, Fig. 10 also exhibits very inaccurate solutions for the VEM due to volumetric locking.

### 6.4. Cook's membrane

This standard benchmark problem is suitable to test the performance of numerical formulations for nearly incompressible solid materials under combined bending and shear. The geometry and boundary conditions for this problem are schematically shown in Fig. 11. There, the left edge is clamped and the right edge is subjected to a shear load $P = 6.25$ N/mm (total shear load of 100 N). The following material parameters are used: $E = 250$ MPa and $\nu = 0.4999$. In this example, a non standard mesh is tested. To this end, we define a master multielement region formed by five polygons, as shown in Fig. 12(a), where the center polygon is an eight-point star known as 'Guñelve'. This master multielement is mapped into the membrane geometry several times to form the mesh. A sample 'Guñelve' mesh is shown in Fig. 12(b).

The convergence of the vertical tip displacement at point A upon mesh refinement is studied. For comparison purposes, a reference solution for the vertical tip displacement is found using a
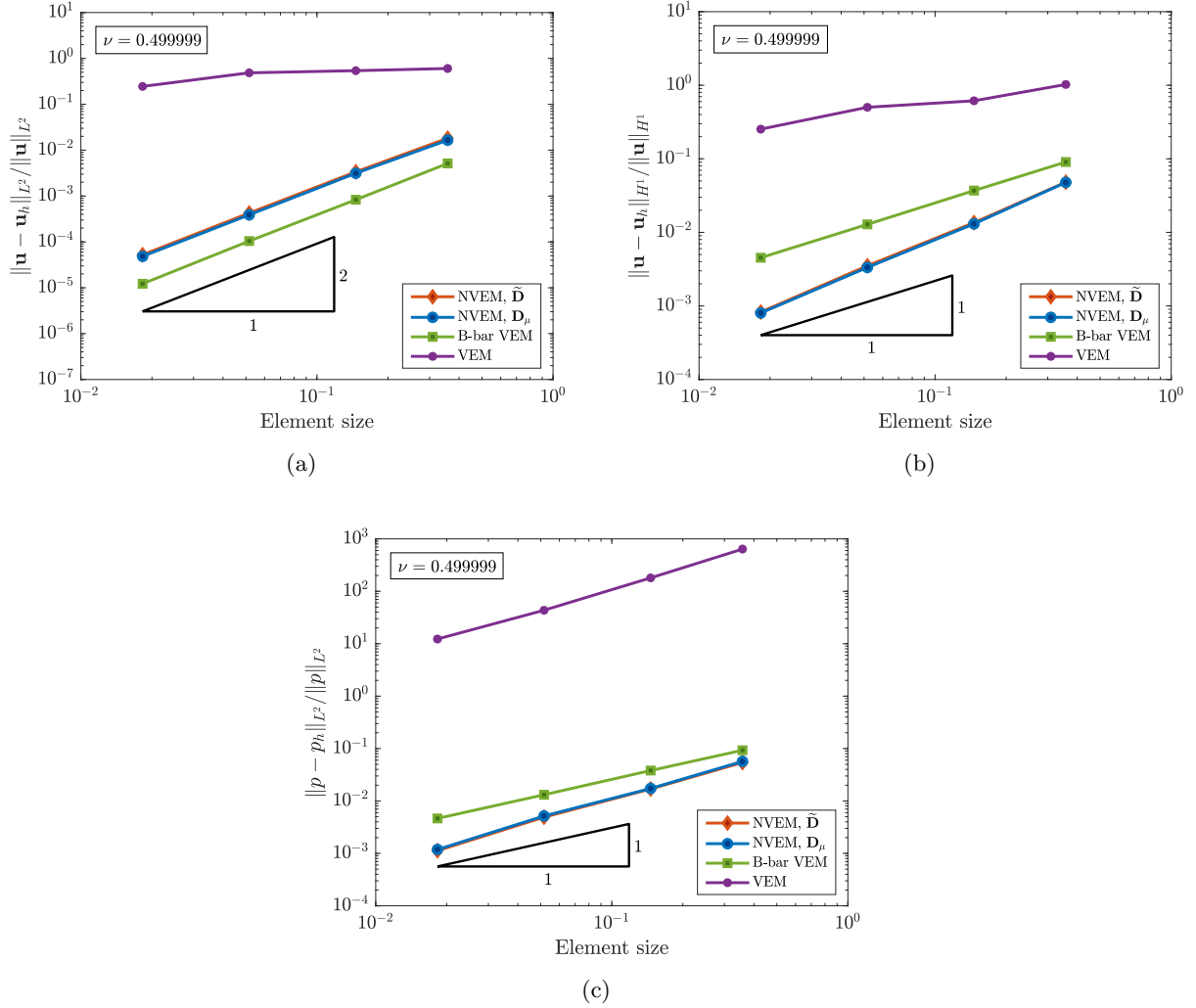
27
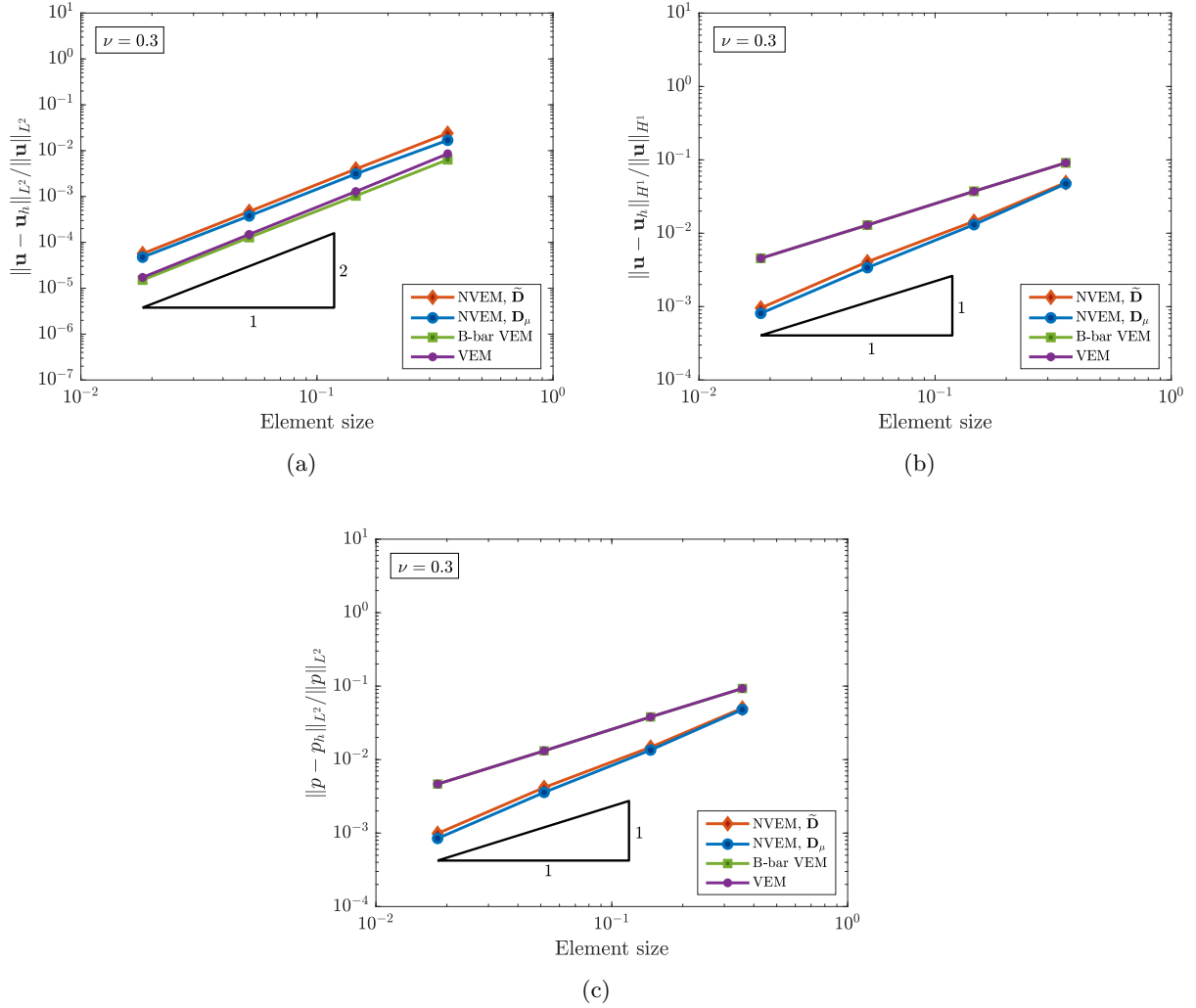
Fig. 9: Cantilever beam problem with material parameters $E_Y = 10^7$ psi and $\nu = 0.3$. Convergence rates in the (a) $L^2$ norm of the displacement error, (b) $H^1$ seminorm of the displacement error and (c) $L^2$ norm of the pressure error for the VEM, B-bar VEM and NVEM.

highly refined mesh of eight-node quadrilateral finite elements. The result of this study is summarized in Fig. 13, where it is shown that the B-bar VEM and the NVEM solutions approach the reference value as the mesh is refined, and, as expected, the standard VEM exhibits very poor convergence due to volumetric locking.

Plots of the vertical displacement, pressure and von Mises stress fields are presented in Figs. 14, 15 and 16, respectively. Scatter plots are used for the NVEM as in this approach the field variables are known at the nodes. As expected, a very good agreement between the NVEM and

28

Fig. 10: Cantilever beam problem with material parameters $E_Y = 10^7$ psi and $\nu = 0.499999$. Convergence rates in the (a) $L^2$ norm of the displacement error, (b) $H^1$ seminorm of the displacement error and (c) $L^2$ norm of the pressure error for the VEM, B-bar VEM and NVEM.

the B-bar VEM solutions is observed in these plots.

## 6.5. Infinite plate with a circular hole

This example is devoted to study an infinite plate with a circular hole that is loaded at infinity with the following tractions: $\sigma_{11} = T$ and $\sigma_{22} = \sigma_{12} = 0$ (see Fig. 17(a)). Due to the symmetry of the geometry and boundary conditions, a quarter of the domain is used as the domain of analysis (see Fig. 17(b)). Plane stress and plane strain conditions are considered. For plane stress condition, the material parameters are set to $E_Y = 10^3$ psi and $\nu = 0.3$ (compressible elasticity), and for plane

29
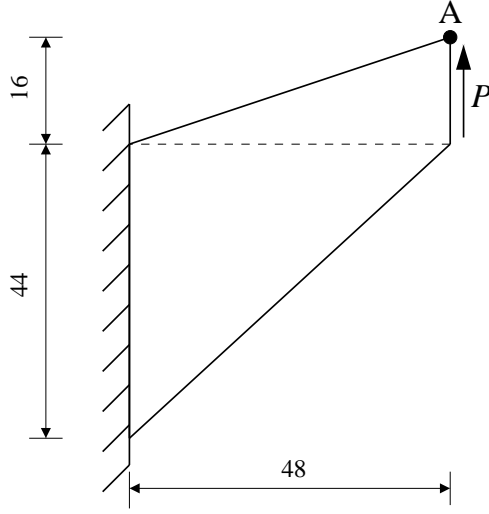
Fig. 11: Geometry and boundary conditions for the Cook's membrane problem (dimensions in mm).



(a)



(b)
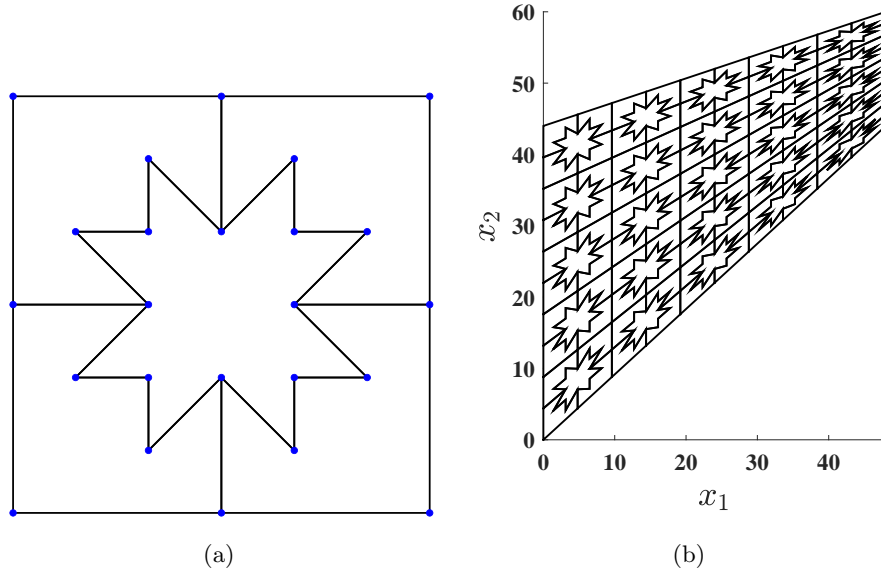
Fig. 12: Cook's membrane problem. (a) Master multielement. The center polygon defines an eight-point star known as 'Guñelve'; (b) a sample 'Guñelve' mesh.

strain condition, they are set to $E_\text{Y} = 10^3$ psi and $\nu = 0.499999$ (nearly incompressible elasticity).

The exact solution is given by [84]

$$\mathbf{u} = \begin{bmatrix} \frac{T}{4G}\left( \frac{\kappa+1}{2}r\cos\theta + \frac{r_0^2}{r}\left( (\kappa+1)\cos\theta + \cos 3\theta \right) - \frac{r_0^4}{r^3}\cos 3\theta \right) \\ \frac{T}{4G}\left( \frac{\kappa-3}{2}r\sin\theta + \frac{r_0^2}{r}\left( (\kappa-1)\sin\theta + \sin 3\theta \right) - \frac{r_0^4}{r^3}\sin 3\theta \right) \end{bmatrix},$$

30
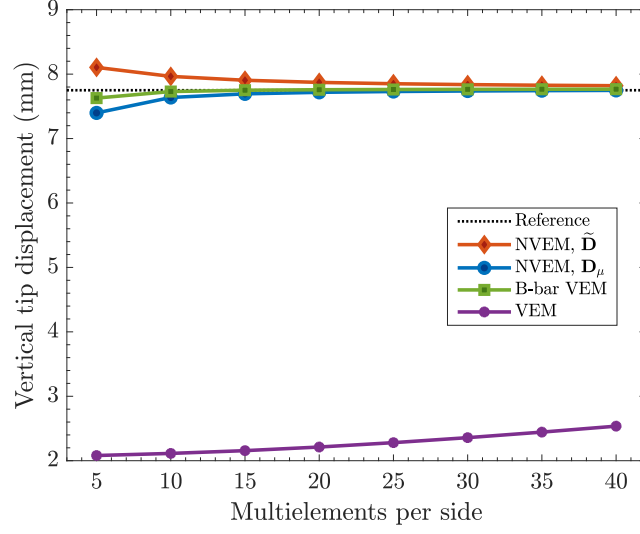
Fig. 13: Convergence of the vertical displacement at the tip of the Cook's membrane (point A) upon mesh refinement for the VEM, B-bar VEM and NVEM.

where $G = E_Y/(2(1 + \nu))$ and $\kappa = (3 - \nu)/(1 + \nu)$. The exact stress field is

$$
\begin{bmatrix} \sigma_{11} \\ \sigma_{22} \\ \sigma_{12} \end{bmatrix} = \begin{bmatrix} T\left(1 - \frac{r_0^2}{r^2}\left(\frac{3}{2}\cos 2\theta + \cos 4\theta\right) + \frac{3r_0^4}{2r^4}\cos 4\theta\right) \\ -T\left(\frac{r_0^2}{r^2}\left(\frac{1}{2}\cos 2\theta - \cos 4\theta\right) + \frac{3r_0^4}{2r^4}\cos 4\theta\right) \\ -T\left(\frac{r_0^2}{r^2}\left(\frac{1}{2}\sin 2\theta + \sin 4\theta\right) - \frac{3r_0^4}{2r^4}\sin 4\theta\right) \end{bmatrix},
$$

where $r$ is the radial distance from the center $(x_1 = 0, x_2 = 0)$ to a point $(x_1, x_2)$ in the domain of analysis. In the computations, the following data are used: $T = 100$ psi, $r_0 = 1$ in and $a = 5$ in. The Dirichlet boundary conditions in inches are imposed on the domain of analysis (Fig. 17(b)) as follows: $u_{1D} = 0$ on the left side and $u_{2D} = 0$ on the bottom side. The Neumann boundary conditions are prescribed using the exact stresses, as follows: $\mathbf{t}_N = \begin{bmatrix} t_{1N} & t_{2N} \end{bmatrix}^\mathsf{T} = \begin{bmatrix} \sigma_{12} & \sigma_{22} \end{bmatrix}^\mathsf{T}$ on the top side and $\mathbf{t}_N = \begin{bmatrix} t_{1N} & t_{2N} \end{bmatrix}^\mathsf{T} = \begin{bmatrix} \sigma_{11} & \sigma_{12} \end{bmatrix}^\mathsf{T}$ on the right side.

In this example, regular, distorted and random meshes are used. For each of them, Fig. 18 shows a sample mesh. The random meshes are built using Polylla, a polygonal mesh generator [85]. Polylla generates meshes from any input triangulation (in this case, a Delaunay triangulation) using the longest-edge propagation path [86] and terminal-edge region concepts.
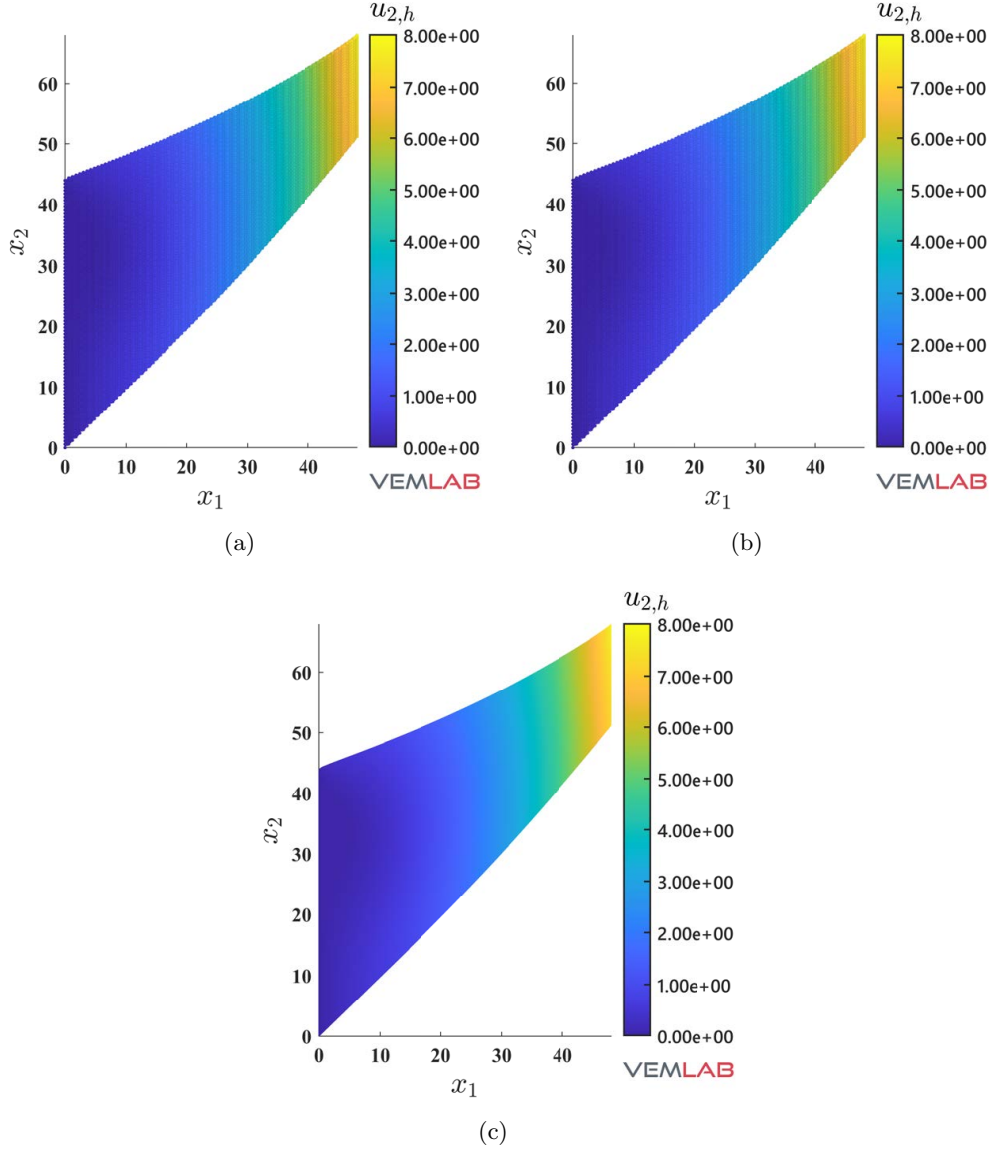
31

Fig. 14: Cook's membrane problem. Plots of the vertical displacement field solution $(u_{2,h})$ in mm for the (a) NVEM ($\tilde{\mathbf{D}}$ stabilization), (b) NVEM ($\mathbf{D}_\mu$ stabilization) and (c) B-bar VEM approaches. Plots are deformed according to $u_{2,h}$.

### 6.5.1. Compressible elasticity

In terms of accuracy and convergence upon mesh refinement, Fig. 19 reveals that for the compressible case on regular meshes all the methods are accurate and converge optimally in the $L^2$ norm and $H^1$ seminorm of the displacement error, and the $L^2$ norm of the pressure error (rates of 2, 1 and 1, respectively). In the $L^2$ norm of the displacement error, the VEM and the B-bar
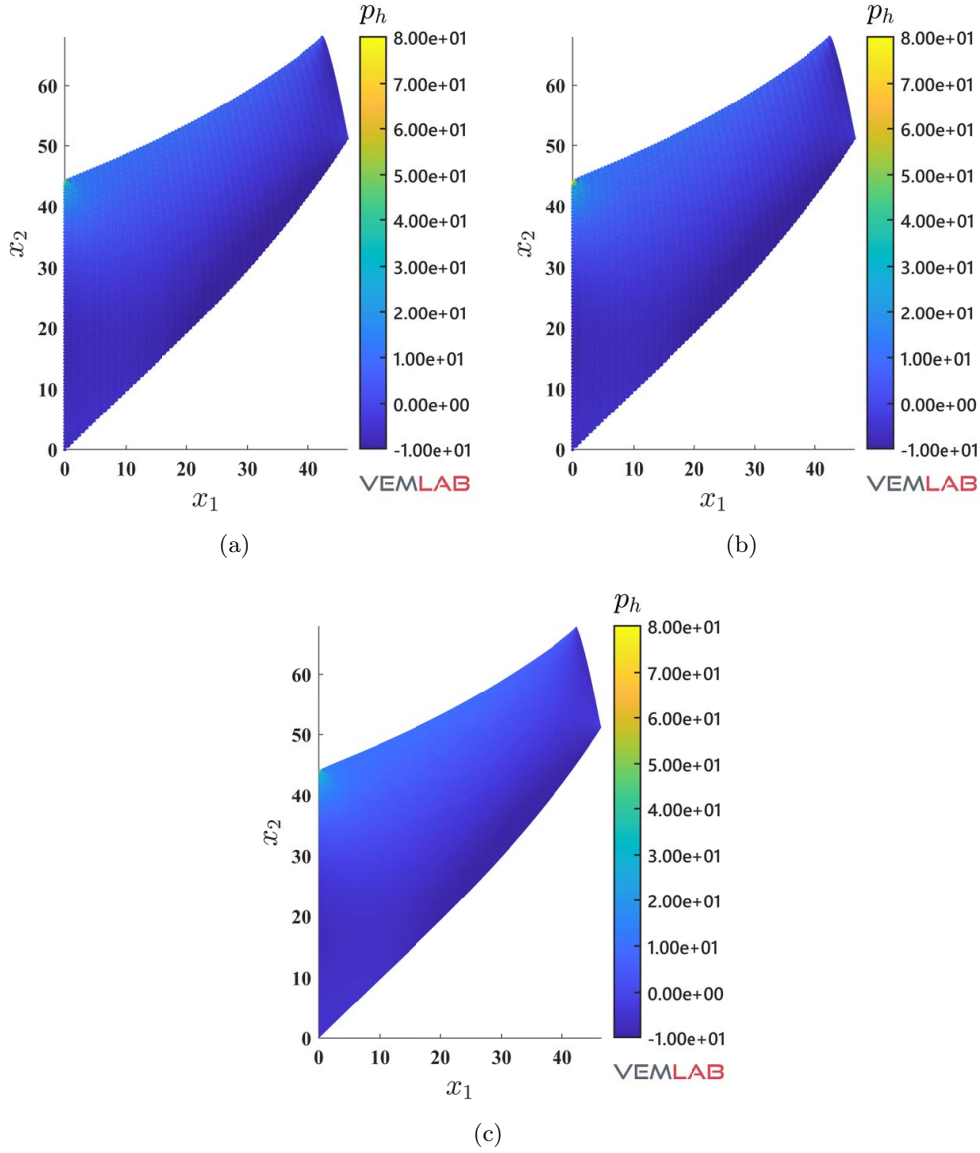
Fig. 15: Cook's membrane problem. Plots of the pressure field solution $(p_h)$ in MPa for the (a) NVEM ($\check{\mathbf{D}}$ stabilization), (b) NVEM ($\mathbf{D}_\mu$ stabilization) and (c) B-bar VEM approaches. Plots are deformed according to $\|\mathbf{u}_h\|$.

VEM are more accurate than the NVEM. In the $H^1$ seminorm of the displacement error and the $L^2$ norm of the pressure error, the VEM, the B-bar VEM and the NVEM with $\widetilde{\mathbf{D}}$ stabilization behave similar, while the NVEM with $\mathbf{D}_\mu$ stabilization delivers the most accurate solution.
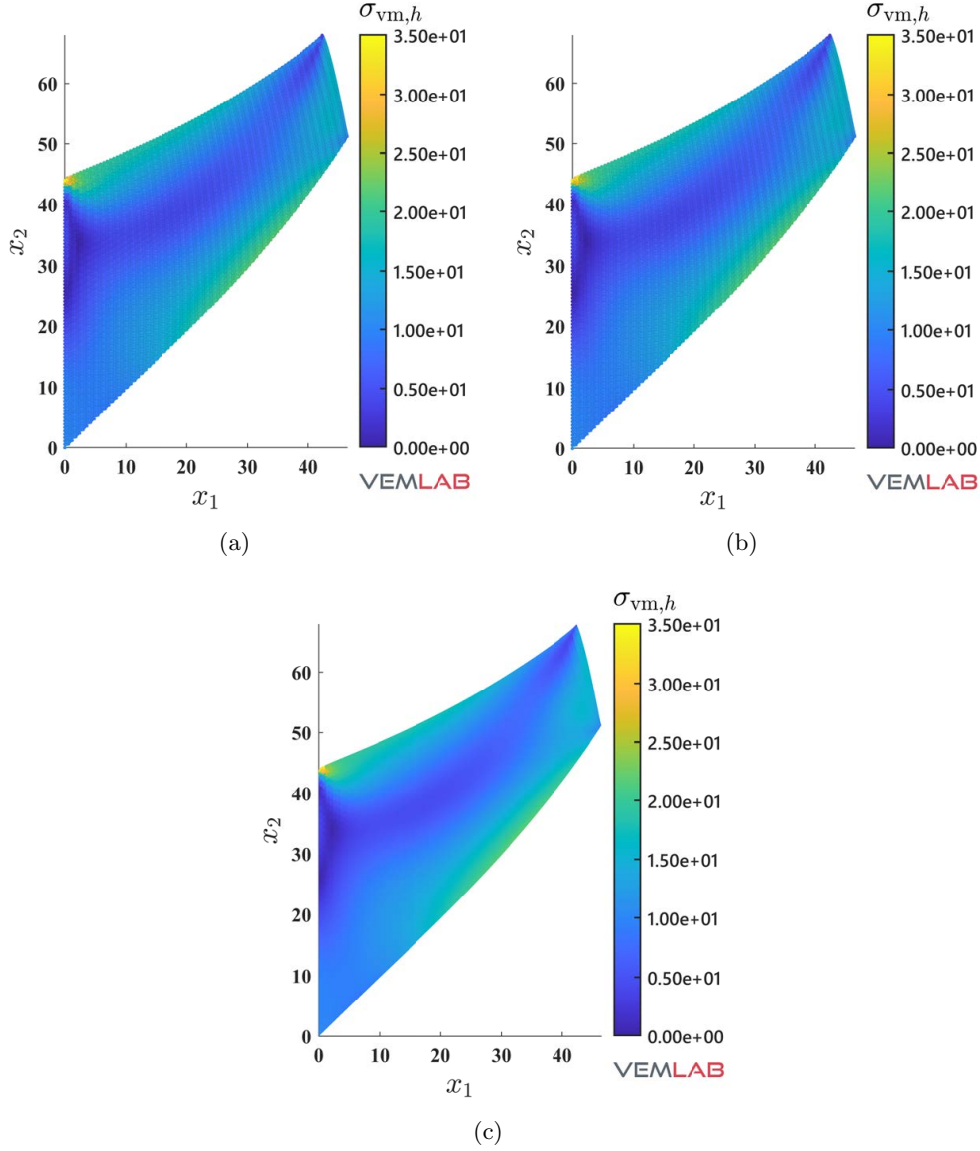
Fig. 16: Cook's membrane problem. Plots of the von Mises stress field solution ($\sigma_{\mathrm{vm},h}$) in MPa for the (a) NVEM ($\tilde{\mathbf{D}}$ stabilization), (b) NVEM ($\mathbf{D}_\mu$ stabilization) and (c) B-bar VEM approaches. Plots are deformed according to $\|\mathbf{u}_h\|$.

### 6.5.2. Nearly incompressible elasticity

For the nearly incompressible case, regular, distorted and random meshes are considered. On regular and distorted meshes, the B-bar VEM and the NVEM are accurate and optimally convergent in the three norms (see Figs. 20 and 21), whereas, as expected, the VEM is severely inaccurate due to volumetric locking. In comparison with the B-bar VEM, Figs. 20 and 21 show that the
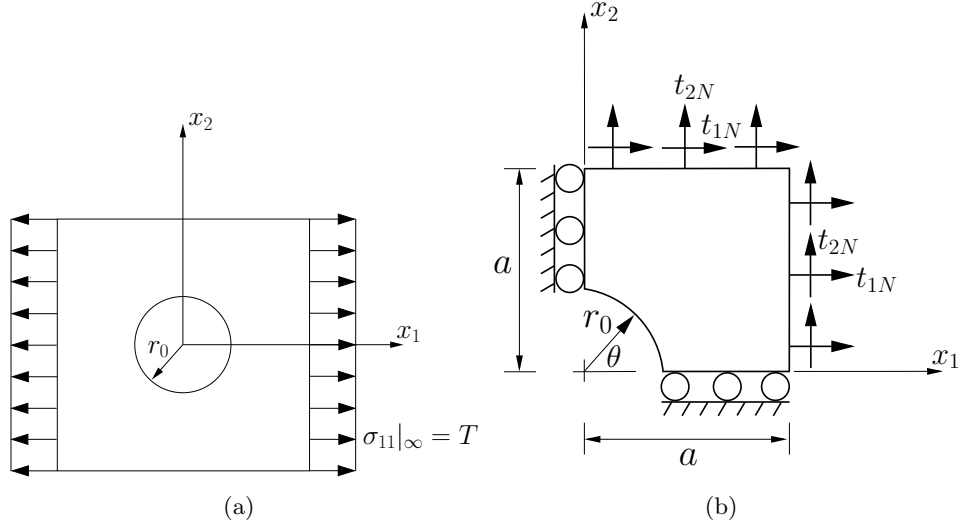
Fig. 17: Geometry and boundary conditions for the infinite plate with a circular hole. (a) Infinite domain and (b) a quarter of the domain.

NVEM is slightly more accurate in the $H^1$ seminorm of the displacement error and the $L^2$ norm of the pressure error, whereas less accurate in the $L^2$ norm of the displacement error. We also observe that between the two stabilized NVEM, the NVEM with $\mathbf{D}_\mu$ stabilization is slightly more accurate.

On random meshes, the B-bar VEM and the NVEM are accurate and optimally convergent in the three norms (Fig. 22), whereas the VEM is severely inaccurate due to volumetric locking. Fig. 22(a) reveals that in the $L^2$ norm of the displacement error the NVEM with $\widetilde{\mathbf{D}}$ stabilization is less accurate than the B-bar VEM, whereas slightly more accurate when $\mathbf{D}_\mu$ stabilization is used. Regarding the $H^1$ seminorm of the displacement error, Fig. 22(b) shows that the B-bar VEM and the NVEM with $\widetilde{\mathbf{D}}$ stabilization behave similar, while the NVEM with $\mathbf{D}_\mu$ stabilization is the most accurate. With respect to the $L^2$ norm of the pressure error, the B-bar VEM is slightly more accurate than the NVEM approach (Fig. 22(c)).

Finally, plots of the displacement, pressure and von Mises stress fields are presented in Figs. 23, 24 and 25, respectively. Scatter plots are used for the NVEM as in this approach the field variables are known at the nodes. A very good agreement between the NVEM and the B-bar VEM solutions is found in these plots.
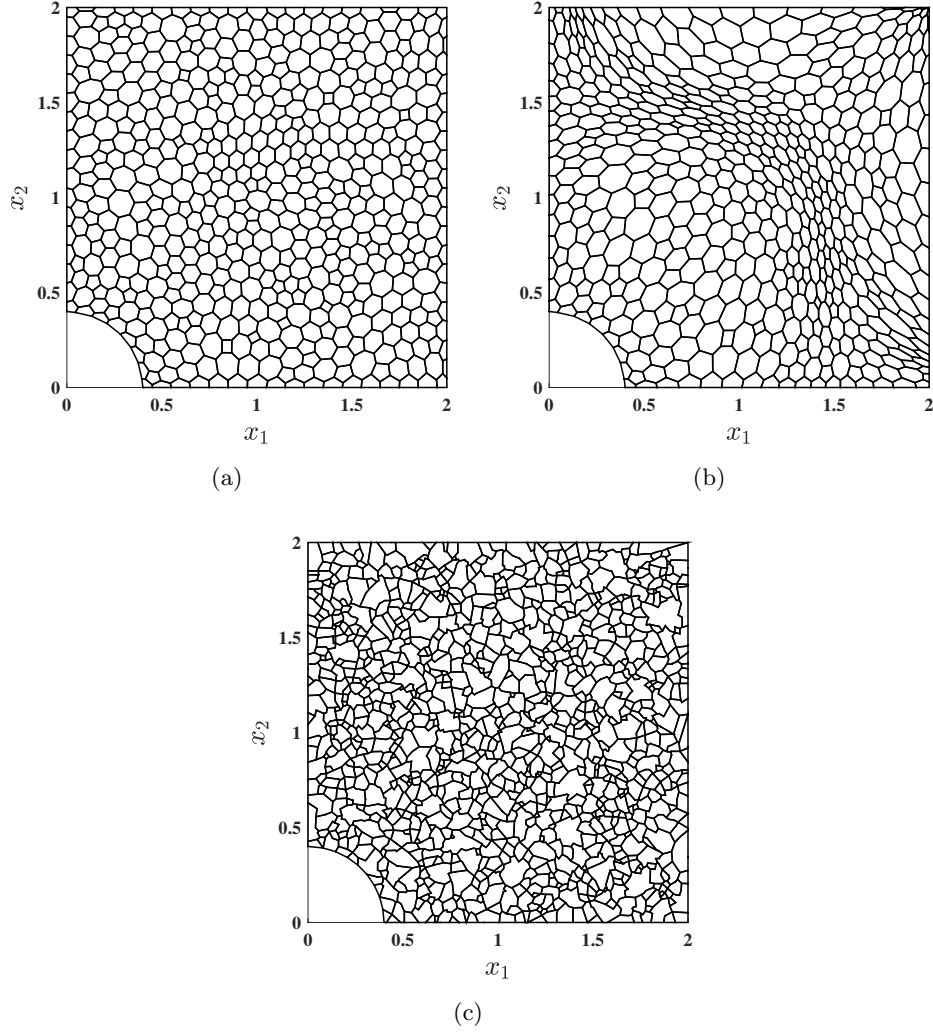
35

Fig. 18: Sample meshes for a quarter of the infinite plate with a circular hole. (a) Regular, (b) distorted and (c) random meshes.

### 6.6. Dynamic response of a cantilever beam

The last numerical example aims to assess the NVEM approach in an elastodynamic analysis of a cantilever beam subjected to a point force that is applied at the tip of the beam. Three cases are considered for the tip load: a constant impact load, a variable impact load and a harmonic load. The body force due to the acceleration of gravity is present at all times in the analysis. The beam geometry and boundary conditions are shown in Fig. 26. Four meshes of increasing density are considered, which are shown in Fig. 27. For each of the three cases considered, a reference solution is obtained with a highly refined mesh of eight-node quadrilateral finite elements (FEM,
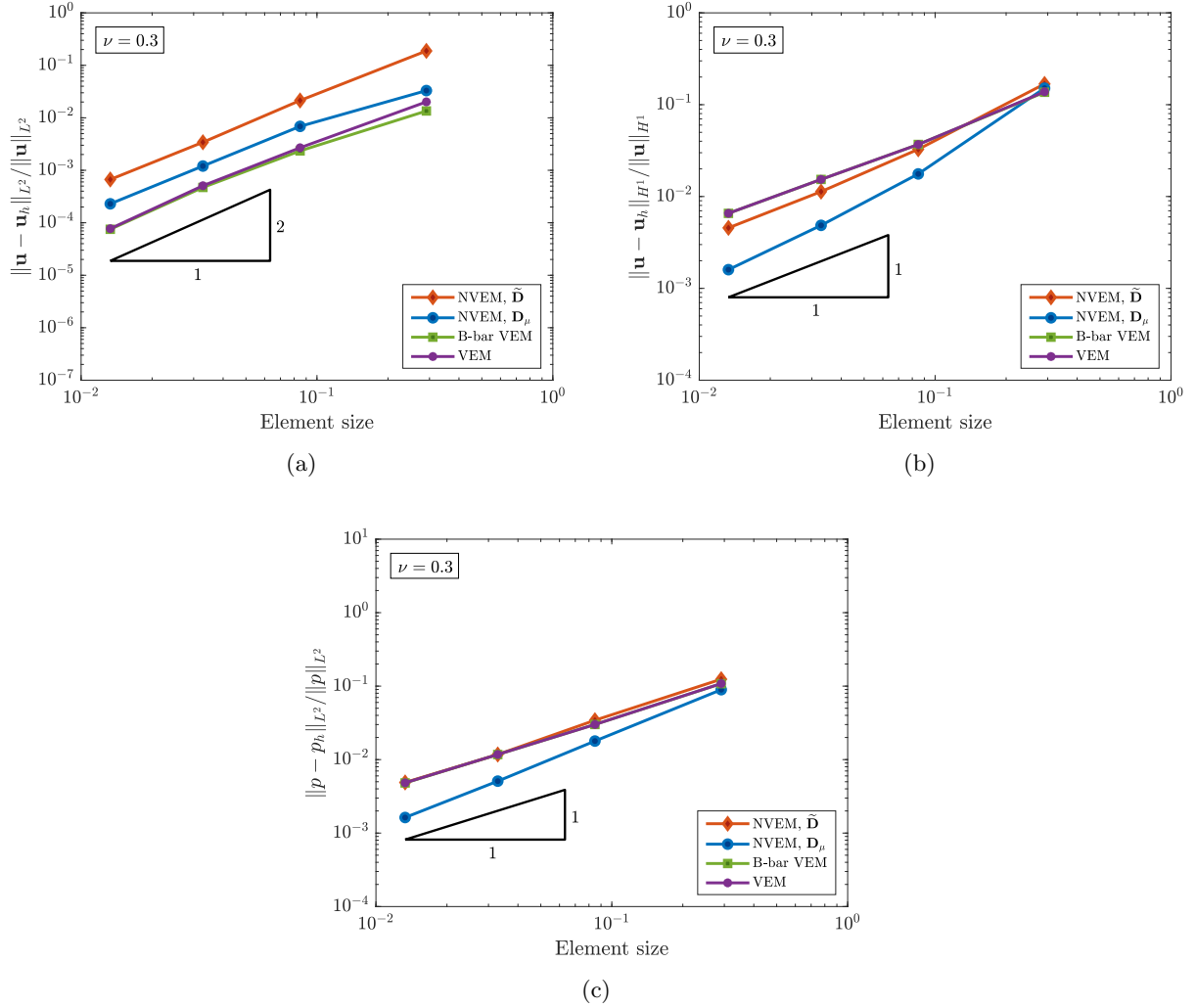
36

Fig. 19: Infinite plate with a circular hole problem on regular meshes. Material parameters $E_Y = 10^3$ psi and $\nu = 0.3$ for plane stress condition. Convergence rates in the (a) $L^2$ norm of the displacement error, (b) $H^1$ seminorm of the displacement error and (c) $L^2$ norm of the pressure error for the VEM, B-bar VEM and NVEM.

Q8) consisting of 62850 degrees of freedom.

The semidiscrete equation of motion of the elastodynamic problem is given by [87]

$$\mathbf{M}\ddot{\mathbf{d}} + \mathbf{C}\dot{\mathbf{d}} + \mathbf{K}\mathbf{d} = \mathbf{F},$$

where $\mathbf{M}$ is the global mass matrix, $\mathbf{C}$ is the global viscous damping matrix, $\mathbf{K}$ is the global stiffness matrix, $\mathbf{F}$ is the global vector of external forces, and $\ddot{\mathbf{d}}$, $\dot{\mathbf{d}}$ and $\mathbf{d}$ are the nodal accelerations, nodal
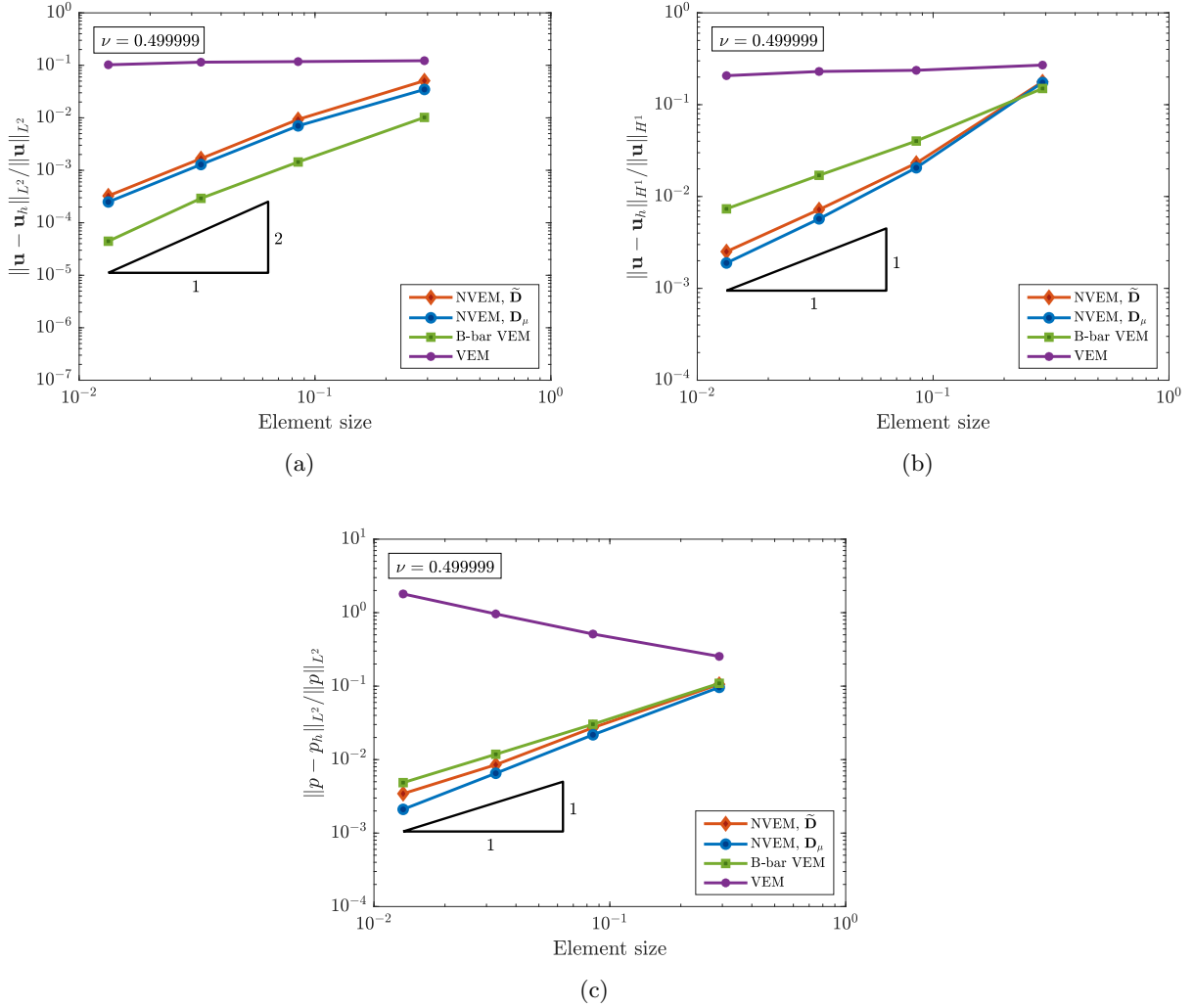
Fig. 20: Infinite plate with a circular hole problem (regular meshes). Material parameters $E_Y = 10^3$ psi and $\nu = 0.499999$ for plane strain condition. Convergence rates in the (a) $L^2$ norm of the displacement error, (b) $H^1$ seminorm of the displacement error and (c) $L^2$ norm of the pressure error for the VEM, B-bar VEM and NVEM.

velocities and nodal displacements, respectively. In the NVEM, $\mathbf{K}$ and $\mathbf{F}$ are formed, respectively, by assembling the element matrices $\mathbf{K}_I$ and $\mathbf{f}_I$ that were developed in the preceding sections. The element mass matrix for the NVEM can be constructed following the construction of the element mass matrix for the VEM as given in Ref. [88], which, in the notation used in the present article, is:

$$(\mathbf{M}_E)_{ab} = \rho \left( \int_E \varPi\phi_a \varPi\phi_b \, d\mathbf{x} + |E| \left[ (\mathbf{I} - \mathbf{P})^\mathsf{T}(\mathbf{I} - \mathbf{P}) \right]_{ab} \right).$$

Notice that applying the averaging operator $\pi_I$ to $\varPi\phi_a$, that is $\pi_I[\varPi\phi_a] = (\varPi\phi_a)_I$, gives a constant
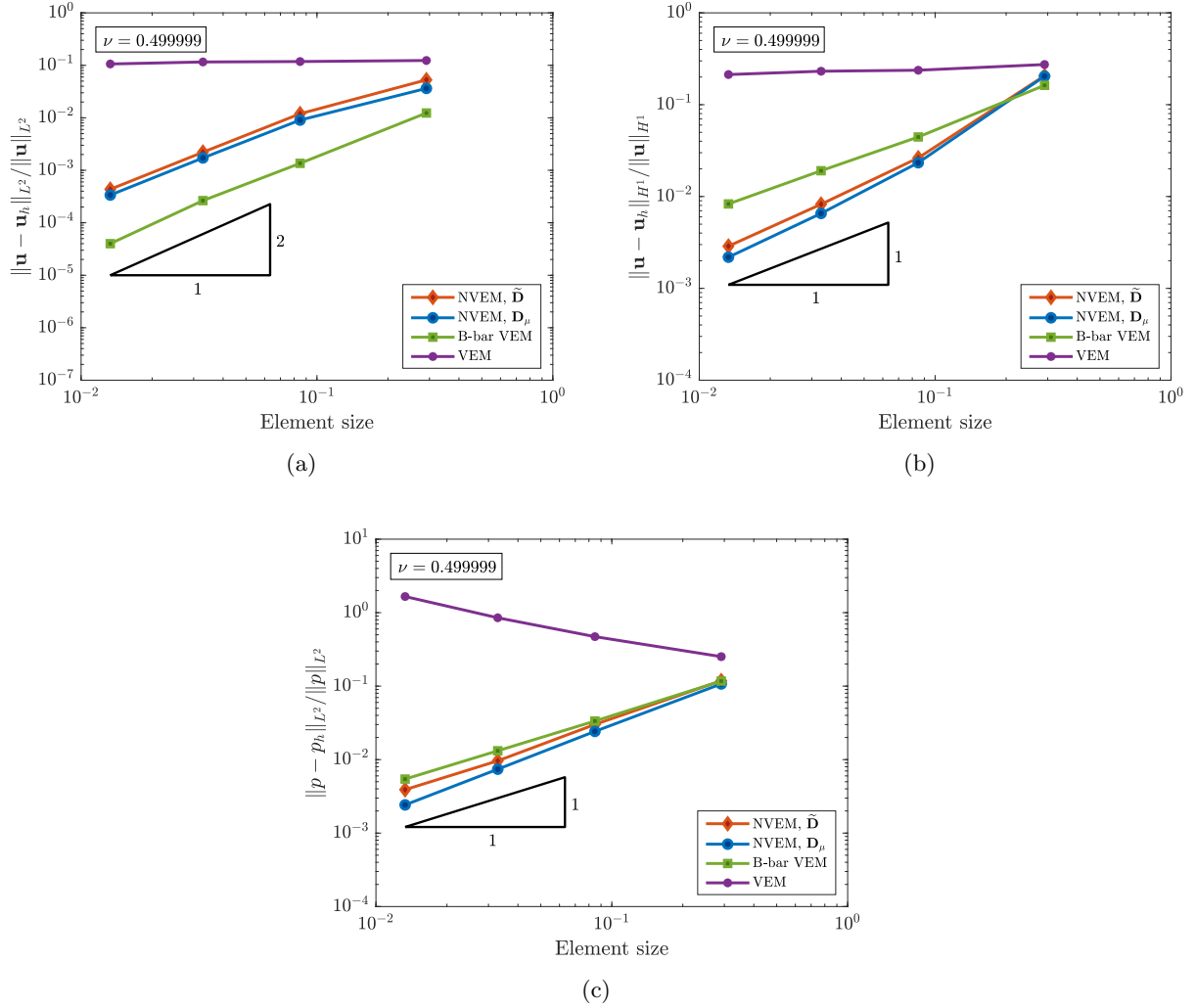
38

Fig. 21: Infinite plate with a circular hole problem (distorted meshes). Material parameters $E_Y = 10^3$ psi and $\nu = 0.499999$ for plane strain condition. Convergence rates in the (a) $L^2$ norm of the displacement error, (b) $H^1$ seminorm of the displacement error and (c) $L^2$ norm of the pressure error for the VEM, B-bar VEM and NVEM.

matrix representing the evaluation of $\Pi\phi_a$ at node $I$. Hence, the NVEM representation of the element mass matrix is written as follows:

$$(\mathbf{M}_I)_{ab} = \rho\,|I|\Big((\Pi\phi_a)_I(\Pi\phi_b)_I + \big[(\mathbf{I} - \mathbf{P})_I^\mathsf{T}(\mathbf{I} - \mathbf{P})_I\big]_{ab}\Big).$$

The damping matrix is estimated using the Rayleigh formula [87]:

$$\mathbf{C} = q_1\mathbf{M} + q_2\mathbf{K},$$
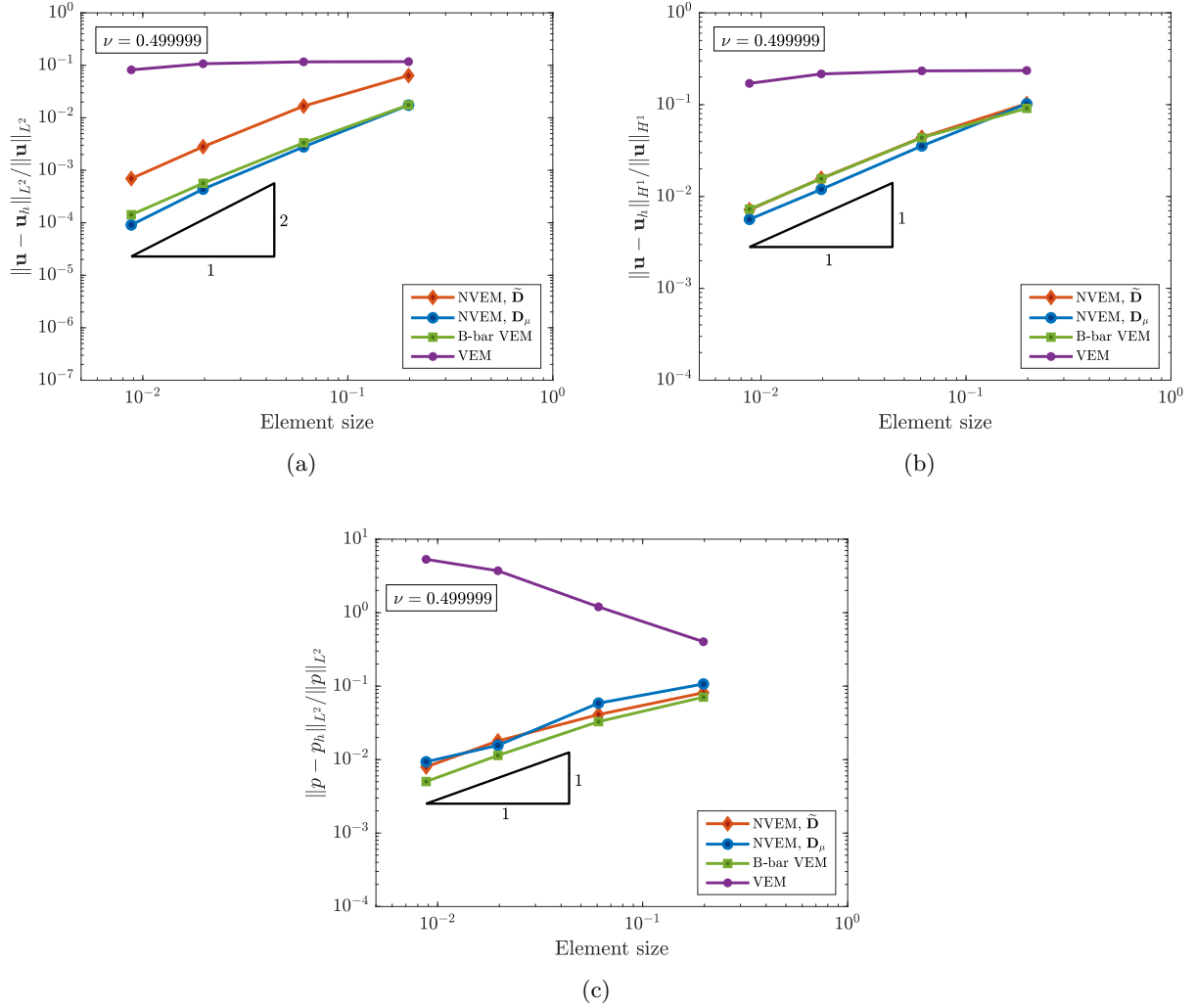
39

(a)



(b)



(c)

Fig. 22: Infinite plate with a circular hole problem (random meshes). Material parameters $E_Y = 10^3$ psi and $\nu = 0.499999$ for plane strain condition. Convergence rates in the (a) $L^2$ norm of the displacement error, (b) $H^1$ seminorm of the displacement error and (c) $L^2$ norm of the pressure error for the VEM, B-bar VEM and NVEM.

where $q_1$ and $q_2$ are constant input parameters. The Hilber-Hughes-Taylor $\alpha$-method [87] is used to solve the semidiscrete equation of motion, which is an implicit, second-order accurate, unconditionally stable algorithm with high-frequency numerical dissipation. The $\alpha$-method leads to the trapezoidal rule for time stepping when the parameter $\alpha$ is set to zero.

The following input data is used for all the simulations performed in this example: $\widetilde{\mathbf{D}}$ stabilization (results are not affected if $\mathbf{D}_\mu$ stabilization is chosen instead), plane stress assumption, beam thickness 20 mm, Young's modulus $E_Y = 200000$ MPa, Poisson's ratio $\nu = 0.3$, mass density
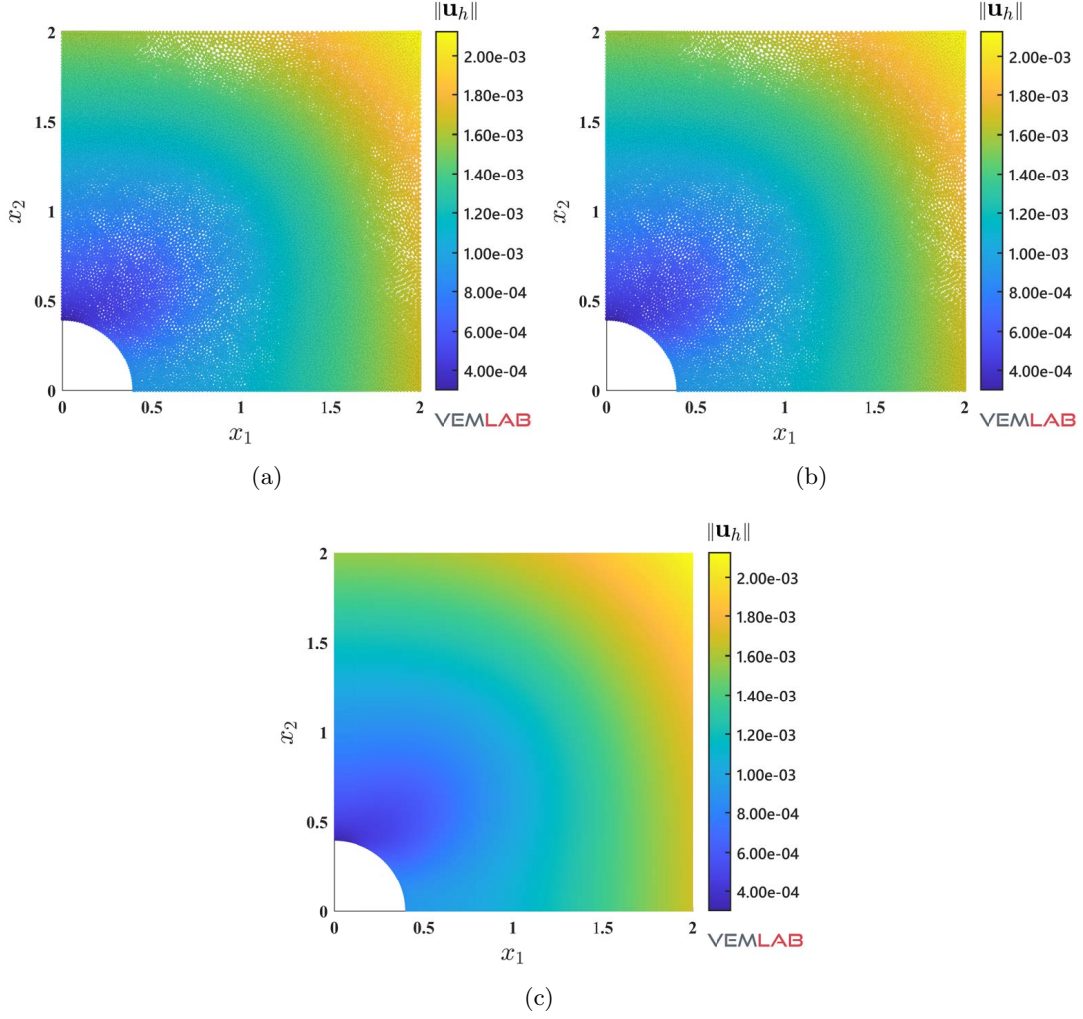
40

Fig. 23: Infinite plate with a circular hole problem. Material parameters $E_Y = 10^3$ psi and $\nu = 0.499999$ for plane strain condition. Plots of the norm of the displacement field solution ($\|\mathbf{u}_h\|$) in inches for the (a) NVEM ($\tilde{\mathbf{D}}$ stabilization), (b) NVEM ($\mathbf{D}_\mu$ stabilization) and (c) B-bar VEM approaches.

$\rho = 7.85 \times 10^{-9}$ t/mm$^3$, acceleration of gravity $g = 9800$ mm/s$^2$, Rayleigh damping parameters $q_1 = 0.025$ and $q_2 = 0.001$, $\alpha$-method parameter $\alpha = -0.1$, time interval in seconds [0, 1.6], time step $\Delta t = 0.001$ s — the time step is chosen according to the usual rule that the period associated with the lowest natural frequency is at least 30 times the time step size. Using the Euler-Bernoulli theory to estimate the lowest natural frequency gives 18.12 hz; hence, the step size is chosen such that $\Delta t < (1/18.12)/30 = 0.0018$ s.
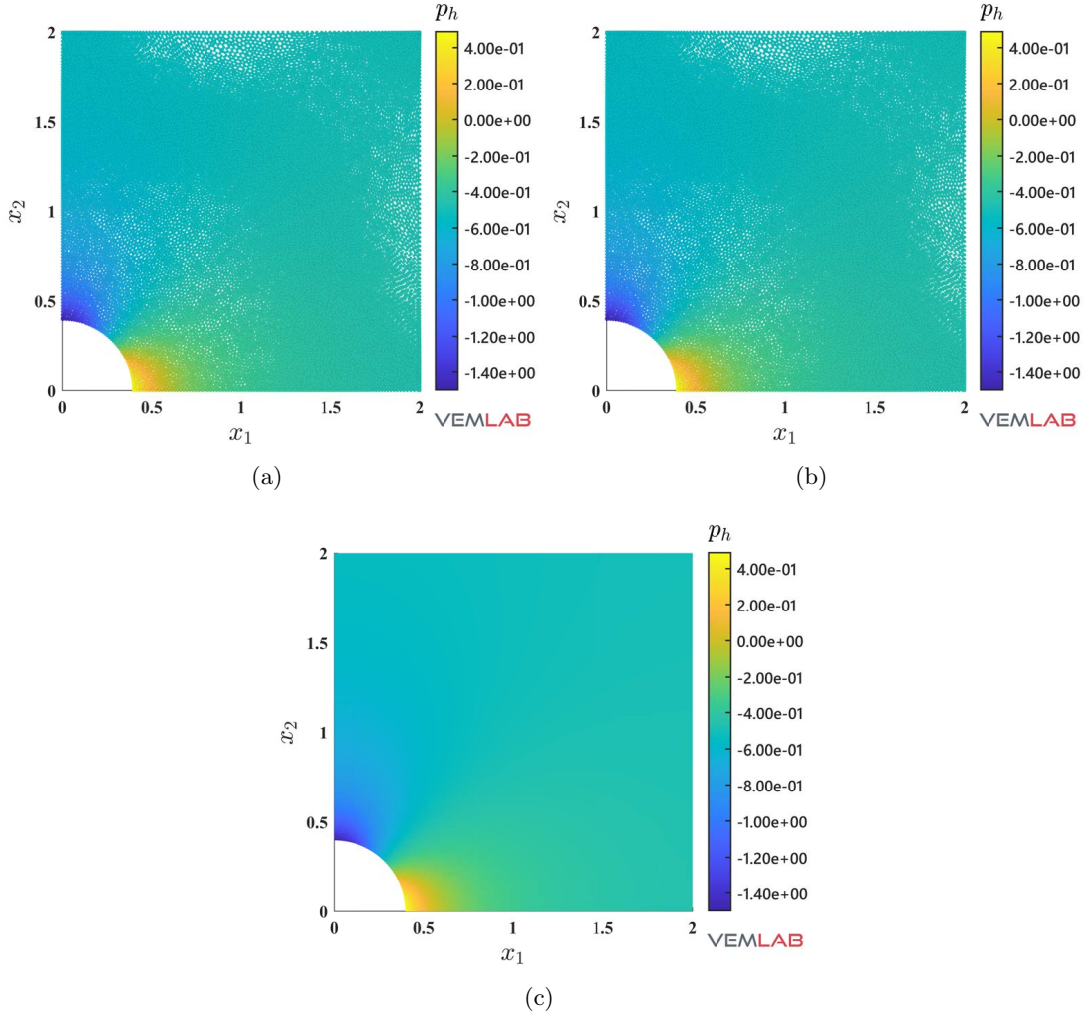
Fig. 24: Infinite plate with a circular hole problem. Material parameters $E_Y = 10^3$ psi and $\nu = 0.499999$ for plane strain condition. Plots of the pressure field solution $(p_h)$ in psi for the (a) NVEM ($\tilde{\mathbf{D}}$ stabilization), (b) NVEM ($\mathbf{D}_\mu$ stabilization) and (c) B-bar VEM approaches.

### 6.6.1. Constant impact load

The beam is initially undeformed and at rest. A constant impact load $P = -10000$ N is applied at time $t = 0$ s at the tip of the beam (point $A$) and is assumed to remain fixed throughout the time interval of analysis. Fig. 28 presents the response curves at point $A$ for the meshes shown in Fig. 27. As expected, it is observed that with mesh refinement the accuracy of the dynamic response increases. In particular, the finer mesh (mesh (d)) matches very well with the reference finite element dynamic response.
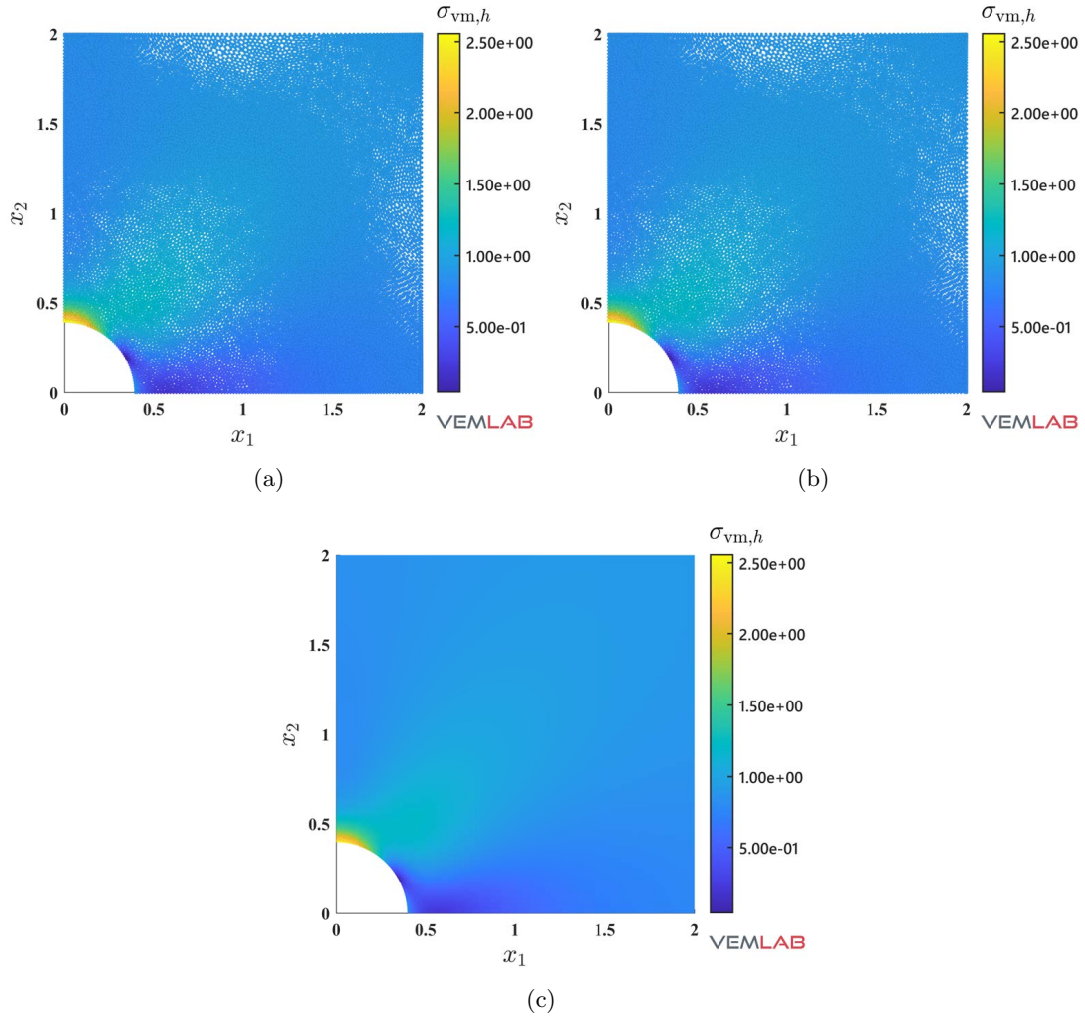
Fig. 25: Infinite plate with a circular hole problem. Material parameters $E_Y = 10^3$ psi and $\nu = 0.499999$ for plane strain condition. Plots of the von Mises stress field solution ($\sigma_{\mathrm{vm},h}$) in psi for the (a) NVEM ($\tilde{\mathbf{D}}$ stabilization), (b) NVEM ($\mathbf{D}_\mu$ stabilization) and (c) B-bar VEM approaches.
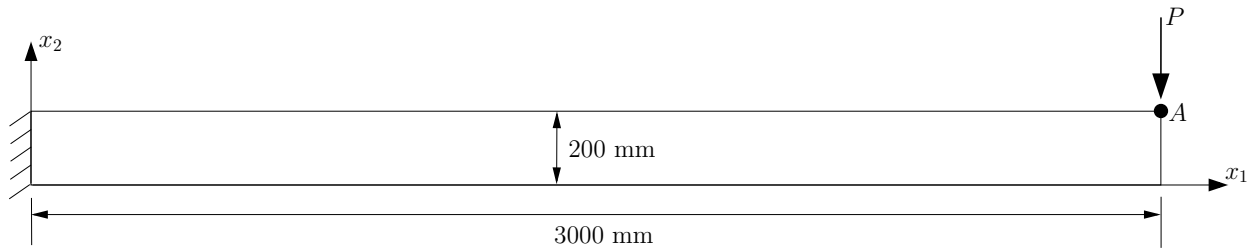


Fig. 26: Geometry and boundary conditions for the dynamic response of a cantilever beam problem.
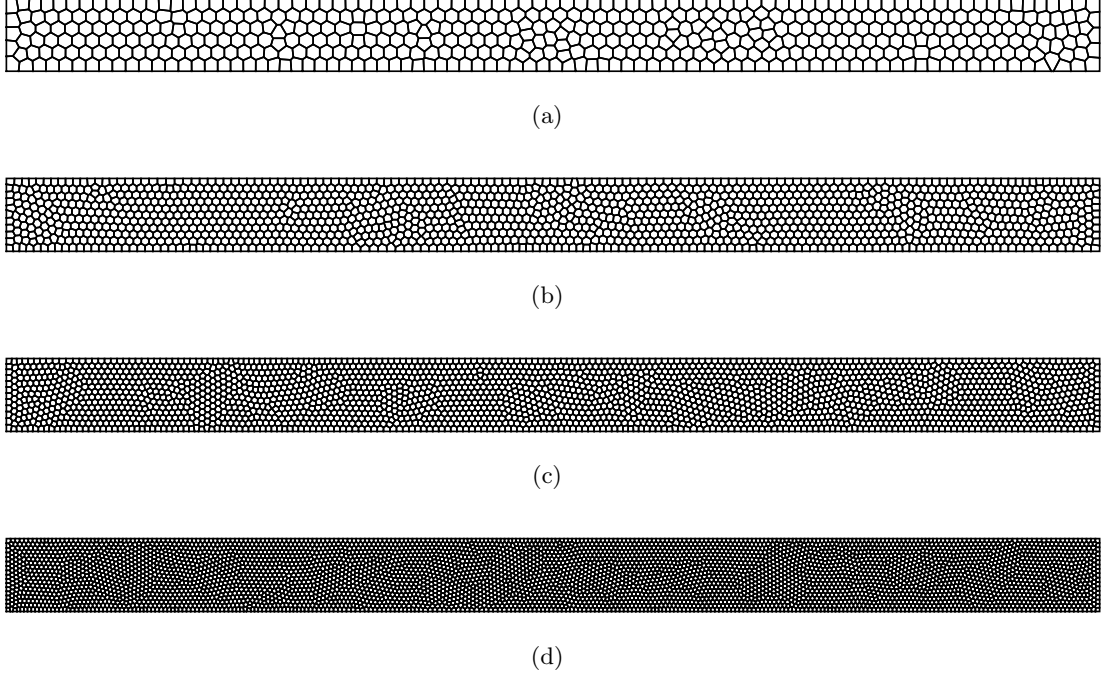
Fig. 27: Meshes for the dynamic response of a cantilever beam. (a) 500 polygonal elements (2004 degrees of freedom), (b) 1500 polygonal elements (6004 degrees of freedom), (c) 2500 polygonal elements (10002 degrees of freedom) and (d) 5000 polygonal elements (20000 degrees of freedom).
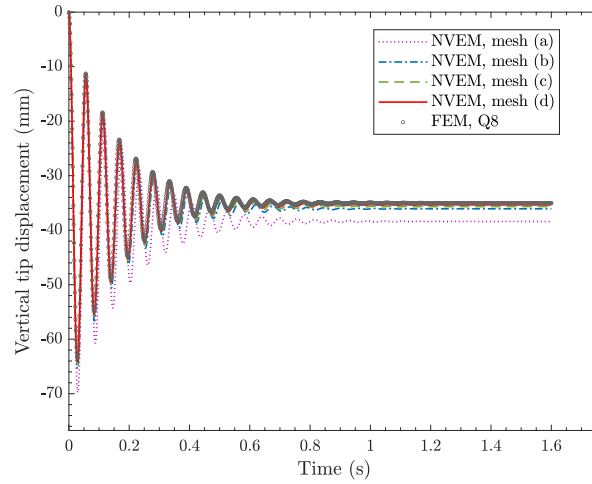


Fig. 28: Dynamic response of the cantilever beam subjected to a constant impact tip load. Comparison among the response curves at the tip of beam for the NVEM using four meshes of increasing density and a reference response curve obtained with 8-node quadrilateral finite elements (FEM, Q8).

*6.6.2. Variable impact load*

The beam is initially undeformed and at rest. The impact load at the tip of the beam (point $A$) is $P = f(t)F$, where $F = -10000$ N and $f(t)$ is defined as

44

$$
f(t) = \begin{cases} -500t + 1, & 0 \leq t \leq 0.002 \\ \\ 0, & t > 0.002 \end{cases}
$$

Fig. 29 presents the response curves at point $A$ for the meshes shown in Fig. 27. It is observed that the accuracy of the dynamic response increases with mesh refinement and that the finer mesh (mesh (d)) matches very well with the reference finite element dynamic response.
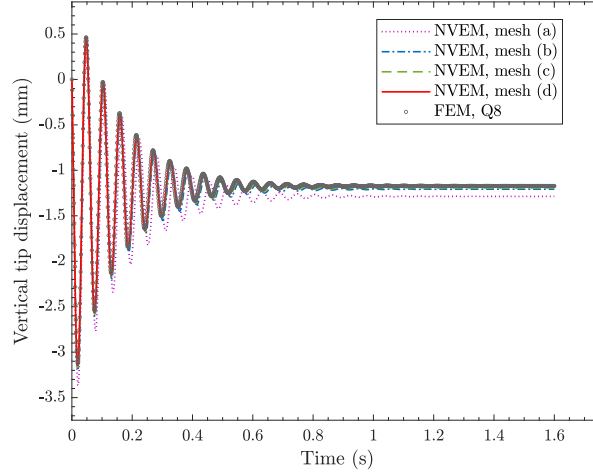


Fig. 29: Dynamic response of the cantilever beam subjected to a variable impact tip load. Comparison among the response curves at the tip of beam for the NVEM using four meshes of increasing density and a reference response curve obtained with 8-node quadrilateral finite elements (FEM, Q8).

### 6.6.3. Harmonic load

The beam is initially undeformed and at rest. A harmonic load defined as $P = -10000 \cos{(\omega_f t)}$ N, where $\omega_f = 8$ rad/s, is applied at point $A$. Fig. 30 depicts the response curves at point $A$ for the meshes shown in Fig. 27. As in the two preceding load cases, the results show that the accuracy of the dynamic response increases with mesh refinement. Among the meshes considered, the finer mesh (mesh (d)) provides the best agreement with the reference finite element dynamic response.

## 7. Concluding remarks

In this paper, we proposed a combined nodal integration and virtual element method, wherein the strain is averaged at the nodes from the strain of surrounding virtual elements. For the strain averaging procedure, a nodal averaging operator was constructed using a generalization to virtual elements of the node-based uniform strain approach for finite elements [64]. This gave rise to the node-based uniform strain virtual element method (NVEM). In line with nodal integration
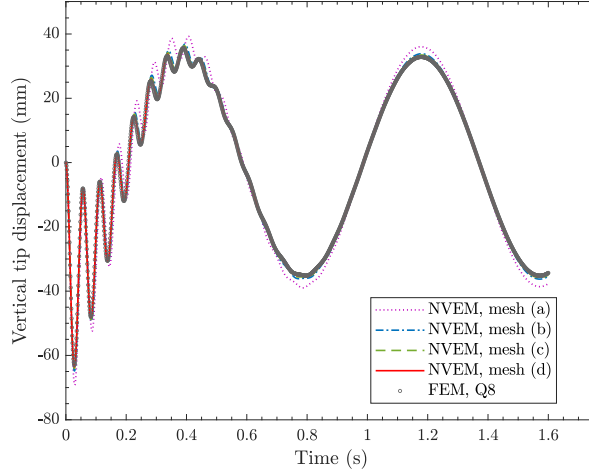
Fig. 30: Dynamic response of the cantilever beam subjected to a harmonic tip load. Comparison among the response curves at the tip of beam for the NVEM using four meshes of increasing density and a reference response curve obtained with 8-node quadrilateral finite elements (FEM, Q8).

techniques, two stabilizations were proposed for the NVEM using modified constitutive matrices. The main distinction between the NVEM and existing VEM approaches for compressible and nearly incompressible elasticity, such as the B-Bar VEM [7], is that the stresses and strains in the NVEM are nodal variables just like displacements, whereas in the existing methods the stresses and strains are element variables.

Several examples in compressible and nearly incompressible elasticity were conducted using regular, distorted and random discretizations in two dimensions. The NVEM showed accurate, convergent and stable solutions in the $L^2$ norm and $H^1$ seminorm of the displacement error in all the numerical tests. An elastodynamic numerical experiment was also conducted for the NVEM. The dynamic response of the NVEM was found to be in good agreement with reference solutions obtained with 8-node quadrilateral finite elements. Even though the NVEM and the B-Bar VEM behave similar in terms of accuracy and convergence, we remark that all the field variables in the NVEM are related to the nodes, which would obviously ease the tracking of the state and history-dependent variables in the nonlinear regime. Also, as in meshfree methods and with the state and history-dependent variables stored at the nodes, the NVEM would be suitable for large deformations settings with remeshing if a remeshing strategy were designed such that the connectivity is revaluated while retaining the current set of nodes. This would obviate the remapping of state and

46

history-dependent variables between the old and new meshes making the method very attractive. The aforementioned features provide room for further development of the NVEM. In the short term perspective, our current work on the NVEM is focused on its extension to materially-nonlinear-only formulation. In the medium term, we plan to develop its extension to large deformations with remeshing.

**Acknowledgements**

## Appendix A. List of main symbols

$\mathbf{b}$      body force vector

$\widehat{\mathbf{b}}$      element average of the body force vector

$\widehat{\mathbf{b}}_I$      nodal average of $\widehat{\mathbf{b}}$

$\mathbf{D}$      constitutive matrix for the linear elastic material

$\widetilde{\mathbf{D}}$      modified constitutive matrix for the linear elastic material

$\mathbf{D}_\mu$      modified constitutive matrix for the linear elastic material

$E$      element or domain of the element

$e$      edge of an element

$|E|$      area of the element

$|e|$      length of an element edge

$E_{\mathrm{Y}}$      Young's modulus of the linear elastic material

$\mathbf{f}_E^b$      VEM element force vector associated with $\mathbf{b}$

$\mathbf{f}_I^b$      NVEM nodal force vector associated with $\mathbf{b}$

$\mathbf{f}_e^t$      VEM element force vector associated with $\mathbf{t}_N$

$\mathbf{f}_I^t$      NVEM nodal force vector associated with $\mathbf{t}_N$

$I$      a node of the mesh

$|I|$      representative area of node $I$

$\mathbf{K}_E$      VEM element stiffness matrix

$\mathbf{K}_I$      NVEM nodal stiffness matrix

$\mathbf{K}_E^{\mathrm{c}}$      consistency part of the VEM element stiffness matrix

$\mathbf{K}_I^{\mathrm{c}}$      consistency part of the NVEM nodal stiffness matrix

$\mathbf{K}_E^{\mathrm{s}}$      stability part of the VEM element stiffness matrix

$\mathbf{K}_I^{\mathrm{s}}$      stability part of the NVEM nodal stiffness matrix

$\mathbf{M}_I$      NVEM nodal mass matrix

$\mathbf{n}$      unit outward normal to the element boundary

$\mathbf{n}_a$      unit outward normal to the $a$-th edge of the element

$\mathbf{n}_\Gamma$      unit outward normal to the domain boundary

$N_E^V$     number of edges/nodes of an element

$N_e^V$     number of nodes of an element edge

$\mathbf{t}_N$     Neumann boundary condition

$\widehat{\mathbf{t}}_N$     edge average of the Neumann boundary condition

$\widehat{\mathbf{t}}_{N,I}$     nodal average of $\widehat{\mathbf{t}}_N$

$\mathbf{u}$     displacement vector

$\mathbf{u}_D$     Dirichlet boundary condition

$\mathbf{u}_h$     discrete trial displacement vector

$\mathbf{u}_a$     nodal displacement vector

$\bar{\mathbf{u}}$     mean of the values that $\mathbf{u}$ takes over the vertices of an element

$\mathbf{v}$     test displacement vector

$\mathbf{v}_h$     discrete test displacement vector

$\mathbf{x}$     position vector

$\mathbf{x}_a$     nodal coordinates vector

$\bar{\mathbf{x}}$     mean of the values that $\mathbf{x}$ takes over the vertices of an element

$\boldsymbol{\varepsilon}$     small strain tensor

$\widehat{\boldsymbol{\varepsilon}}$     element average of the small strain tensor

$\boldsymbol{\varepsilon}_I$     nodal strain tensor

$\partial E$     boundary of the element

$\Gamma$     boundary of the body

$\Gamma_D$     Dirichlet boundary

$\Gamma_N$     Neumann boundary

$\lambda$     Lamé's first parameter

$\mu$     Lamé's second parameter (shear modulus of the linear elastic material)

$\nu$     Poisson's ratio of the linear elastic material

$\Omega$     domain of the body

$\boldsymbol{\omega}$     small rotation tensor

$\widehat{\boldsymbol{\omega}}$     element average of the small rotation tensor

$\boldsymbol{\sigma}$     Cauchy stress tensor

[1] L. Beirão da Veiga, F. Brezzi, A. Cangiani, G. Manzini, L. D. Marini, A. Russo, Basic principles of virtual element methods, Mathematical Models and Methods in Applied Sciences 23 (1) (2013) 199–214.

[2] A. Cangiani, G. Manzini, A. Russo, N. Sukumar, Hourglass stabilization and the virtual element method, International Journal for Numerical Methods in Engineering 102 (3–4) (2015) 404–436.

[3] L. Beirão da Veiga, F. Brezzi, L. D. Marini, Virtual elements for linear elasticity problems, SIAM Journal on Numerical Analysis 51 (2) (2013) 794–812.

[4] L. Beirão da Veiga, C. Lovadina, D. Mora, A Virtual Element Method for elastic and inelastic problems on polytope meshes, Computer Methods in Applied Mechanics and Engineering 295 (2015) 327–346.

[5] E. Artioli, L. Beirão da Veiga, C. Lovadina, E. Sacco, Arbitrary order 2D virtual elements for polygonal meshes: part I, elastic problem, Computational Mechanics 60 (3) (2017) 355–377.

[6] E. Artioli, L. Beirão da Veiga, C. Lovadina, E. Sacco, Arbitrary order 2D virtual elements for polygonal meshes: part II, inelastic problem, Computational Mechanics 60 (4) (2017) 643–657.

[7] K. Park, H. Chi, G. H. Paulino, B-bar virtual element method for nearly incompressible and compressible materials, Meccanica 56 (6) (2021) 1423–1439.

[8] A. L. Gain, C. Talischi, G. H. Paulino, On the virtual element method for three-dimensional linear elasticity problems on arbitrary polyhedral meshes, Computer Methods in Applied Mechanics and Engineering 282 (2014) 132–160.

[9] A. D'Altri, S. de Miranda, L. Patruno, E. Sacco, An enhanced vem formulation for plane elasticity, Computer Methods in Applied Mechanics and Engineering 376 (2021) 113663.

[10] X. Tang, Z. Liu, B. Zhang, M. Feng, A low-order locking-free virtual element for linear elasticity problems, Computers & Mathematics with Applications 80 (5) (2020) 1260–1274.

[11] M. Cihan, B. Hudobivnik, F. Aldakheel, P. Wriggers, 3D mixed virtual element formulation for dynamic elasto-plastic analysis, Computational Mechanics 68 (3) (2021) 1–18.

[12] K. Park, H. Chi, G. H. Paulino, Numerical recipes for elastodynamic virtual element methods with explicit time integration, International Journal for Numerical Methods in Engineering 121 (1) (2020) 1–31.

[13] K. Park, H. Chi, G. H. Paulino, On nonconvex meshes for elastodynamics using virtual element methods with explicit time integration, Computer Methods in Applied Mechanics and Engineering 356 (2019) 669–684.

[14] P. Wriggers, W. T. Rust, A virtual element method for frictional contact including large deformations, Engineering Computations 36 (7) (2019) 2133–2161.

[15] M. De Bellis, P. Wriggers, B. Hudobivnik, Serendipity virtual element formulation for nonlinear elasticity, Computers & Structures 223 (2019) 106094.

[16] F. Aldakheel, B. Hudobivnik, P. Wriggers, Virtual elements for finite thermo-plasticity problems, Computational Mechanics 64 (5) (2019) 1347–1360.

[17] P. Wriggers, B. Hudobivnik, A low order virtual element formulation for finite elasto-plastic deformations, Computer Methods in Applied Mechanics and Engineering 327 (2017) 459–477.

[18] P. Wriggers, B. D. Reddy, W. Rust, B. Hudobivnik, Efficient virtual element formulations for compressible and incompressible finite deformations, Computational Mechanics 60 (2) (2017) 253–268.

[19] B. Hudobivnik, F. Aldakheel, P. Wriggers, A low order 3D virtual element formulation for finite elasto–plastic deformations, Computational Mechanics 63 (2) (2019) 253–269.

[20] X. Zhang, H. Chi, G. Paulino, Adaptive multi-material topology optimization with hyperelastic materials under large deformations: A virtual element approach, Computer Methods in Applied Mechanics and Engineering 370 (2020) 112976.

[21] H. Chi, L. Beirão da Veiga, G. Paulino, Some basic formulations of the virtual element method (VEM) for finite deformations, Computer Methods in Applied Mechanics and Engineering 318 (2017) 148–192.

[22] D. van Huyssteen, B. Reddy, A virtual element method for isotropic hyperelasticity, Computer Methods in Applied Mechanics and Engineering 367 (2020) 113134.

[23] P. Wriggers, W. T. Rust, B. D. Reddy, A virtual element method for contact, Computational Mechanics 58 (6) (2016) 1039–1050.

[24] F. Aldakheel, B. Hudobivnik, E. Artioli, L. Beirão da Veiga, P. Wriggers, Curvilinear virtual elements for contact mechanics, Computer Methods in Applied Mechanics and Engineering 372 (2020) 113394.

[25] F. Aldakheel, B. Hudobivnik, P. Wriggers, Virtual element formulation for phase-field modeling of ductile fracture, International Journal for Multiscale Computational Engineering 17 (2) (2019) 181–200.

[26] A. Hussein, F. Aldakheel, B. Hudobivnik, P. Wriggers, P.-A. Guidault, O. Allix, A computational framework for brittle crack-propagation based on efficient virtual element method, Finite Elements in Analysis and Design 159 (2019) 15–32.

[27] V. Nguyen-Thanh, X. Zhuang, H. Nguyen-Xuan, T. Rabczuk, P. Wriggers, A Virtual Element Method for 2d linear elastic fracture analysis, Computer Methods in Applied Mechanics and Engineering 340 (2018) 366–395.

[28] M. Benedetto, A. Caggiano, G. Etse, Virtual elements and zero thickness interface-based approach for fracture analysis of heterogeneous materials, Computer Methods in Applied Mechanics and Engineering 338 (2018) 41–67.

[29] E. Artioli, S. Marfia, E. Sacco, VEM-based tracking algorithm for cohesive/frictional 2d fracture, Computer Methods in Applied Mechanics and Engineering 365 (2020) 112956.

[30] L. Beirão da Veiga, A. Pichler, G. Vacca, A virtual element method for the miscible displacement of incompressible fluids in porous media, Computer Methods in Applied Mechanics and Engineering 375 (2021) 113649.

[31] L. Chen, F. Wang, A Divergence Free Weak Virtual Element Method for the Stokes Problem on Polytopal Meshes, Journal of Scientific Computing 78 (2) (2019) 864–886.

[32] G. Gatica, M. Munar, F. Sequeira, A mixed virtual element method for the Navier–Stokes equations, Mathematical Models and Methods in Applied Sciences 28 (14) (2018) 2719–2762.

[33] L. Beirão da Veiga, C. Lovadina, G. Vacca, Virtual elements for the Navier–Stokes problem on polygonal meshes, SIAM Journal on Numerical Analysis 56 (3) (2018) 1210–1242.

[34] A. Chernov, C. Marcati, L. Mascotto, p- and hp- virtual elements for the Stokes problem, Advances in Computational Mathematics 47 (2) (2021) 24.

[35] O. Andersen, H. Nilsen, X. Raynaud, Virtual element method for geomechanical simulations of reservoir models, Computational Geosciences 21 (5) (2017) 877–893.

[36] S. Lin, H. Zheng, W. Jiang, W. Li, G. Sun, Investigation of the excavation of stony soil slopes using the virtual element method, Engineering Analysis with Boundary Elements 121 (2020) 76–90.

[37] A. L. Gain, G. H. Paulino, Bridging art and engineering using Escher-based virtual elements, Structural and Multidisciplinary Optimization 51 (2015) 867–883.

[38] H. Chi, A. Pereira, I. F. M. Menezes, G. H. Paulino, Virtual element method (VEM)-based topology optimization: an integrated framework, Structural and Multidisciplinary Optimization 62 (3) (2020) 1089–1114.

[39] E. Artioli, S. de Miranda, C. Lovadina, L. Patruno, A stress/displacement virtual element method for plane elasticity problems, Computer Methods in Applied Mechanics and Engineering 325 (2017) 155–174.

[40] F. Dassi, C. Lovadina, M. Visinoni, Hybridization of the virtual element method for linear elasticity problems, Mathematical Models and Methods in Applied Sciences 31 (14) (2021) 2979–3008.

[41] D. Y. Kwak, H. Park, Lowest-order virtual element methods for linear elasticity problems, Computer Methods in Applied Mechanics and Engineering 390 (2022) 114448.

[42] B. Zhang, J. Zhao, Y. Yang, S. Chen, The nonconforming virtual element method for elasticity problems, Journal of Computational Physics 378 (2019) 394–410.

[43] Y. Yu, A lowest-order locking-free nonconforming virtual element method based on the reduced integration technique for linear elasticity problems, https://arxiv.org/abs/2112.13378 (2021). doi:10.48550/ARXIV.2112.13378.

[44] S. Beissel, T. Belytschko, Nodal integration of the element-free Galerkin method, Computer Methods in Applied Mechanics and Engineering 139 (1) (1996) 49–74.

[45] M. A. Puso, J.-S. Chen, E. Zywicz, W. Elmer, Meshfree and finite element nodal integration methods, International Journal for Numerical Methods in Engineering 74 (3) (2008) 416–446.

[46] T. Belytschko, S. Xiao, Stability analysis of particle methods with corrected derivatives, Computers & Mathematics with Applications 43 (3–5) (2002) 329–350.

[47] T. P. Fries, T. Belytschko, Convergence and stabilization of stress-point integration in mesh-free and particle methods, International Journal for Numerical Methods in Engineering 74 (7) (2008) 1067–1087.

[48] T. Belytschko, Y. Guo, W. K. Liu, S. P. Xiao, A unified stability analysis of meshless particle methods, International Journal for Numerical Methods in Engineering 48 (9) (2000) 1359–1400.

[49] M. Hillman, J.-S. Chen, An accelerated, convergent, and stable nodal integration in Galerkin meshfree methods for linear and nonlinear mechanics, International Journal for Numerical Methods in Engineering 107 (7) (2016) 603–630.

[50] J.-S. Chen, M. Hillman, M. Rüter, An arbitrary order variationally consistent integration for Galerkin meshfree

methods, International Journal for Numerical Methods in Engineering 95 (5) (2013) 387–418.

[51] M. A. Puso, J. Solberg, A stabilized nodally integrated tetrahedral, International Journal for Numerical Methods in Engineering 67 (6) (2006) 841–867.

[52] J.-S. Chen, C. T. Wu, S. Yoon, Y. You, A stabilized conforming nodal integration for Galerkin mesh-free methods, International Journal for Numerical Methods in Engineering 50 (2) (2001) 435–466.

[53] J.-S. Chen, S. Yoon, C. T. Wu, Non-linear version of stabilized conforming nodal integration for Galerkin mesh-free methods, International Journal for Numerical Methods in Engineering 53 (12) (2002) 2587–2615.

[54] W. Elmer, J. S. Chen, M. Puso, E. Taciroglu, A stable, meshfree, nodal integration method for nearly incompressible solids, Finite Elements in Analysis and Design 51 (2012) 81–85.

[55] R. Silva-Valenzuela, A. Ortiz-Bernardin, N. Sukumar, E. Artioli, N. Hitschfeld-Kahler, A nodal integration scheme for meshfree galerkin methods using the virtual element decomposition, International Journal for Numerical Methods in Engineering 121 (10) (2020) 2174–2205.

[56] Q. Duan, B. Wang, X. Gao, X. Li, Quadratically consistent nodal integration for second order meshfree Galerkin methods, Computational Mechanics 54 (2) (2014) 353–368.

[57] P. Lancaster, K. Salkauskas, Surfaces generated by moving least squares methods, Mathematics of Computations 37 (1981) 141–158.

[58] T. Belytschko, Y. Y. Lu, L. Gu, Element-free Galerkin methods, International Journal for Numerical Methods in Engineering 37 (2) (1994) 229–256.

[59] W. K. Liu, S. Jun, Y. F. Zhang, Reproducing kernel particle methods, International Journal for Numerical Methods in Engineering 20 (8–9) (1995) 1081–1106.

[60] N. Sukumar, Construction of polygonal interpolants: a maximum entropy approach, International Journal for Numerical Methods in Engineering 61 (12) (2004) 2159–2181.

[61] N. Sukumar, R. W. Wright, Overview and construction of meshfree basis functions: from moving least squares to entropy approximants, International Journal for Numerical Methods in Engineering 70 (2) (2007) 181–205.

[62] M. Arroyo, M. Ortiz, Local maximum-entropy approximation schemes: a seamless bridge between finite elements and meshfree methods, International Journal for Numerical Methods in Engineering 65 (13) (2006) 2167–2202.

[63] J. Bonet, A. J. Burton, A simple average nodal pressure tetrahedral element for incompressible and nearly incompressible dynamic explicit applications, Communications in Numerical Methods in Engineering 14 (5) (1998) 437–449.

[64] C. R. Dohrmann, M. W. Heinstein, J. Jung, S. W. Key, W. R. Witkowski, Node-based uniform strain elements for three-node triangular and four-node tetrahedral meshes, International Journal for Numerical Methods in Engineering 47 (9) (2000) 1549–1568.

[65] J. Bonet, H. Marriott, O. Hassan, An averaged nodal deformation gradient linear tetrahedral element for large strain explicit dynamic applications, Communications in Numerical Methods in Engineering 17 (8) (2001) 551–561.

[66] P. Krysl, B. Zhu, Locking-free continuum displacement finite elements with nodal integration, International Journal for Numerical Methods in Engineering 76 (7) (2008) 1020–1043.

[67] G. Castellazzi, P. Krysl, Displacement-based finite elements with nodal integration for reissner–mindlin plates, International Journal for Numerical Methods in Engineering 80 (2) (2009) 135–162.

[68] P. Krysl, H. Kagey, Reformulation of nodally integrated continuum elements to attain insensitivity to distortion, International Journal for Numerical Methods in Engineering 90 (7) (2012) 805–818.

[69] G. Castellazzi, P. Krysl, Patch-averaged assumed strain finite elements for stress analysis, International Journal for Numerical Methods in Engineering 90 (13) (2012) 1618–1635.

[70] M. Broccardo, M. Micheloni, P. Krysl, Assumed-deformation gradient finite elements with nodal integration for nearly incompressible large deformation analysis, International Journal for Numerical Methods in Engineering 78 (9) (2009) 1113–1134.

[71] G. Castellazzi, P. Krysl, I. Bartoli, A displacement-based finite element formulation for the analysis of laminated composite plates, Composite Structures 95 (2013) 518–527.

[72] E. Artioli, G. Castellazzi, P. Krysl, Assumed strain nodally integrated hexahedral finite element formulation for elastoplastic applications, International Journal for Numerical Methods in Engineering 99 (11) (2014) 844–866.

[73] A. Franci, M. Cremonesi, U. Perego, E. O. nate, A lagrangian nodal integration method for free-surface fluid flows, Computer Methods in Applied Mechanics and Engineering 361 (2020) 112816.

[74] J. Meng, X. Zhang, S. Utili, E. Oñate, A nodal-integration based particle finite element method (N-PFEM) to model cliff recession, Geomorphology 381 (2021) 107666.

[75] S. Berrone, A. Borio, F. Marcon, Comparison of standard and stabilization free virtual elements on anisotropic elliptic problems, Applied Mathematics Letters 129 (2022) 107971.

[76] A. Chen, N. Sukumar, Stabilization-free serendipity virtual element method for plane elasticity, Computer Methods in Applied Mechanics and Engineering 404 (2023) 115784.

[77] A. Ortiz-Bernardin, C. Alvarez, N. Hitschfeld-Kahler, A. Russo, R. Silva-Valenzuela, E. Olate-Sanzana, Veamy: an extensible object-oriented C++ library for the virtual element method, Numerical Algorithms 82 (4) (2019) 1189–1220.

[78] L. Beirão da Veiga, F. Dassi, A. Russo, High-order virtual element method on polyhedral meshes, Computers & Mathematics with Applications 74 (5) (2017) 1110–1122.

[79] L. Beirão da Veiga, F. Brezzi, F. Dassi, L. D. Marini, A. Russo, Serendipity virtual elements for general elliptic equations in three dimensions, Chinese Annals of Mathematics, Series B 39 (2018) 315–334.

[80] A. Ortiz-Bernardin, A. Russo, N. Sukumar, Consistent and stable meshfree Galerkin methods using the virtual element decomposition, International Journal for Numerical Methods in Engineering 112 (7) (2017) 655–684.

[81] F. M. Andrade Pires, E. A. de Souza Neto, J. L. de la Cuesta Padilla, An assessment of the average nodal volume formulation for the analysis of nearly incompressible solids under finite strains, Communications in Numerical Methods in Engineering 20 (7) (2004) 569–583.

[82] L. Mascotto, Ill-conditioning in the virtual element method: Stabilizations and bases, Numerical Methods for Partial Differential Equations 34 (4) (2018) 1258–1281.

[83] H. C. Elman, D. J. Silvester, A. J. Wathen, Finite Elements and Fast Iterative Solvers: with Applications in Incompressible Fluid Dynamics, Oxford University Press, Inc, NY, 2006.

[84] S. P. Timoshenko, J. N. Goodier, Theory of Elasticity, 3rd Edition, McGraw-Hill, NY, 1970.

[85] S. Salinas, N. Hitschfeld-Kahler, A. Ortiz-Bernardin, H. Si, Polylla: Polygonal meshing algorithm based on terminal-edge regions, Engineering with Computers 38 (2022) 4545–4567.

[86] M.-C. Rivara, New longest-edge algorithms for the refinement and/or improvement of unstructured triangulations, International Journal for Numerical Methods in Engineering 40 (18) (1997) 3313–3324.

[87] T. J. R. Hughes, The Finite Element Method: Linear Static and Dynamic Finite Element Analysis, Dover Publications, Inc, Mineola, NY, 2000.

[88] L. Beirão da Veiga, F. Brezzi, L. D. Marini, A. Russo, The hitchhiker's guide to the virtual element method, Mathematical Models and Methods in Applied Sciences 24 (08) (2014) 1541–1573.